12-2023

Quantification of Dye Degradation on Titanium Dioxide-Based Membranes

Elizabeth Carol Wood
University of Arkansas-Fayetteville

Quantification of Dye Degradation on Titanium Dioxide-Based Membranes

A thesis submitted in partial fulfillment
of requirements for the degree of
Master of Science in Chemistry

by

Elizabeth Carol Wood
Harding University
Bachelor of Science in Chemistry, 2020

December 2023
University of Arkansas

This thesis is approved for recommendation to the Graduate Council.

Jingyi Chen, Ph.D.
Thesis Director

Colin Heyes, Ph.D.
Committee Member

Z. Ryan Tian, Ph.D.
Committee Member

Feng Wang, Ph.D.
Committee Member

The following signatories attest that all software used in this thesis was legally licensed for use by Elizabeth Carol Wood for research purposes and publication.

Mrs. Elizabeth Carol Wood	Dr. Jingyi Chen, Thesis Director

Abstract

The purpose of this study was to examine the dye degradation on the titanium dioxide (TiO_2)-based membranes. While many studies have shown photocatalytic degradation of dye on TiO_2 in solution, few studies have been reported on the solid TiO_2 substrate. In this work, a new method is developed to quantify the dye degradation on TiO_2-based membranes. A hydrothermal method is used to synthesize the photocatalytic TiO_2 nanofibers; vacuum filtration is applied to fabricate a self-assembled membrane. Silver is incorporated into the nanofibers through in situ reduction before vacuum filtration to fabricate Ag/TiO_2 membrane in an attempt to red shift the material's photoactive range; however, oxidized Ag species, such as Ag_2O and AgOH, are likely incorporated due to the nanofibers' basic environment. The catalytic properties of TiO_2 and Ag/TiO_2 membranes are then evaluated by the dye – methylene blue degradation under different conditions. A digital method by coupling the image-capturing method using a Gel Imaging System and the analysis using ImageJ has been standardized to monitor the dye degradation over time on the membranes. This study successfully calibrates the linear region (0 – 72.3 ng) of methylene blue drop cast on the membranes. The color intensity of two methylene blue droplets' mass (36.3 ng and 49.6 ng) is traced under dark and light conditions. The dye degradation on the membranes follows 1^{st} order reaction kinetics while dye degrades faster on the Ag/TiO_2 membrane than the TiO_2 membrane. This method may potentially be used to quantify other dye degradation on the semiconductor membranes in an effort to develop (photo)catalysts for applications such as water treatment.

Acknowledgements

I would like to thank God for providing me with the educational opportunities I have received and blessing me with a wonderful support system. I would also like to express my genuine thanks to my supervisor, Dr. Jingyi Chen. She was a patient teacher, an empathetic mentor, and one of the most joyful advisors I have had the pleasure to work with.

To Dr. Z. Ryan Tian and his group, thank you for the collaboration, guidance, equipment, and training necessary to complete this study. To Dr. Yong Wang, thank you for allowing me to use the Gel Imaging System and for assisting me develop a quantification method. To Dr. Colin Heyes and Dr. Feng Wang, many thanks for all your support and time. It has been so valuable.

Many thanks to the Chen group, David Thompson, Mei York, Deborah Okyere, Isabelle Ishimwe Nkunda, Yibing Hu, and Ryan Manso for the assistance you provided. Your warm collaboration was always welcoming.

To my undergraduate advisors, Dr. Dennis Province and Dr. Cindy White, you two believed in me, invited me into your research, and connected me with Dr. Chen. Thank you.

I am very grateful to my family for their unwavering support. My parents', grandparents', siblings' encouragement, and prayers spurred me on. To my wonderful husband, thank you for your unyielding support and love. I could not have done this without you.

Dedication

This work is dedicated to my Father in Heaven. God has blessed me beyond measure. In everything I do, I strive to "work heartily, as for the Lord…" (Col 3:23) I owe all to Him. And to my grandfather, Louis Gene Reed, LGR. Granddad, I love you and will miss your mischievous laugh and playful pranks. Thank you for challenging me and supporting me always.

Table of Contents

1. Introduction

With much of the world urbanizing after the Industrial Revolution in the 1920s, environmental pollution has become a rising concern. In the late 1970s, awareness rose as environmentalists realized the damage the earth's ecosystem was experiencing. Since then, scientists and politicians from around the globe have been making concerted efforts to reduce pollution and clean the environment, especially that of wastewater.[1–7] Waterborne diseases are responsible for approximately 3.5 million deaths each year, so developing a method of purification in the most rural areas of the world is very important.[8] One of the obstacles encountered in developing methods is that waste is always produced in either the creation the method or reduction and destruction of pollution. For this reason, renewable materials are the ideal tool to process and reduce pollution via photocatalysis. [2,4,9,10]

1.1 Photocatalysis

In materials science, insulators, conductors, and semiconductors are an important topic of interest because of their unique properties and capabilities. In each of these materials, there exist 3 types of energy bands—filled band, valence band, and the conduction band.[11] A filled band resides between the outermost electron and the nucleus whose energy levels are completely filled by electrons. The valence band is the area between the filled electron orbitals and the band gap. It contains the outermost electrons and may or may not possess empty energy levels. Finally, the conduction band is the area of energy levels beyond the band gap. When electrons are present, they are very highly energized and considered to be free electrons. [1,2,9,12]

Photocatalysis is the process by which a material utilizes photonic energy to drive thermodynamically favorable or unfavorable reactions. As the photon is absorbed by the photoconductive material, the material is catalyzed. This process is called photoexcitation and

causes a reaction with $\Delta G>0$, to proceed with the photon acting as a reactant, allowing the energy of activation to be greater than Gibb's free energy.[1310] The first step in this catalyzed reaction is generating charge carriers, or an electron-hole (e^-/h^+) pair. When a photon strikes the valence band, the electron absorbs the energy. The electron is then able to cross the band gap, a region where there exist no quantized energy levels, and reside in the conduction band leaving an electron/hole pair.[14] These charge carriers can only exist for a matter of nanoseconds before the electron recombines with the electron hole in the valance band.[15] Within that timeframe, redox reactions can occur on the surface of the semiconductor. The electron produces reduction reactions while the positively charged hole produces oxidation reactions. Under high irradiation, multiple electron/hole pairs are created. This produces more active sites and increases the efficiency of the photocatalytic material.[16]

When choosing a photocatalyst, several factors must be considered. Firstly, an ideal photocatalyst is a one that is reusable with little to no decrease in the photocatalytic capability over time. The low-maintenance nature of renewable sources is one of the most attractive qualities when choosing a material. Choosing a photocatalyst that has a long charge carrier lifetime and that produces as little amount of dangerous waste are additional factors to be considered. There are also different types of semiconductors—p-type and n-type. A p-type semiconductor is one whose charge carriers are mostly positive that reside in the valence band. This is a result of the p-type's Fermi level positioned more closely to the valance band. An n-type semiconductor contains a majority of negative charge carriers that reside in the conduction band. N-type semiconductors' Fermi level is closer to the conduction band.[17] This phenomenon assists electrons' excitation and ability of maintain their position in the conduction band. N-type semiconductors are considered excellent photocatalysts.[18] Finally, choosing a material that possesses a band gap that is

photoactive in the visible range rather than ultraviolet is desirable. Not only will this require less energy, but the percentage of visible light in solar radiation is much higher than that of UV light.[18] By adjusting the excitation wavelength of the photocatalyst to the visible light range, the photocatalyst would be more effective in remote areas of the world that do not have easy access to electricity or the ability to purchase battery-operated or solar powered UV source.

The band gap is an important concept and as such, it deserves additional information. A band gap is the area of energy levels in a semiconductor or an insulator where there exist no electrons. This area resides between the highest energy level of the valence band and the lowest energy level of the conduction band.[2,9,10,15,19] To activate the semiconductor, an electron from the valence band must acquire the energy necessary to jump from the valence band to the conduction band. This is commonly done through the exposure of low frequencies of light. Knowing the band gap energy is an important aspect of research and can be discovered through conducting a Tauc Plot analysis of UV-Vis spectra.[20] Before analysis can be discussed, the difference between direct and indirect band gaps must be understood.[19]

Figure 1.1 depicts the key difference between direct and indirect band gaps. The crystal momentum (k-vector) of electrons and holes, where p=E/c vary. The k-vector, also known as the wave-vector, is an important aspect of band gap theory. If the k-vectors of the valence band are in phase with the k-vectors of the conduction band, photon emission is much more attainable. In direct band gaps, the bonding and antibonding possess the same momentum, whereas the indirect band gaps possess electrons and hole pairs that have different momentums.[19] As an electron rises from the valence band, it will need to change its potential and momentum to find the electron hole in the conduction band. Therefore, indirect band gaps are not as efficient as the direct band gap.[9,19]

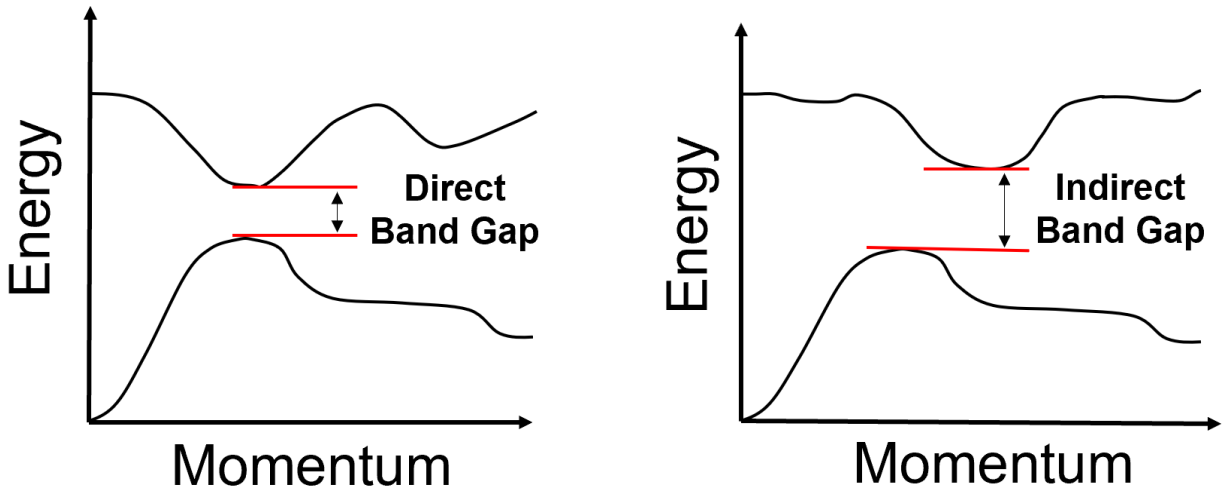

Figure 1.1: Example of direct and indirect band gap.

1.2 TiO_2 as a Semiconductor

Titanium Dioxide (TiO_2) is cheap, commercially available, non-toxic, and is easy to use as a framework for other metals. Due to its non-toxic nature, it is commonly used in batteries, photovoltaic cells, photocatalysis, ion exchange, paint, cosmetics, and paper.[21–26] It possesses high stability and activity, making this semiconductor a popular material for wastewater and hazardous chemical waste disposal. TiO_2 is a photocatalyst that is active in the ultraviolet range and possesses an indirect band gap of 3.2 eV.[14,26,27] The valance band edge has an energy of -7.6 eV under vacuum while the conduction band edge has an energy of -4.4 eV under vacuum. Studies have shown that TiO_2 produces redox reactions when excited by photons of 350 nm to 410 nm, as seen in Figure 1.2. [28–37]

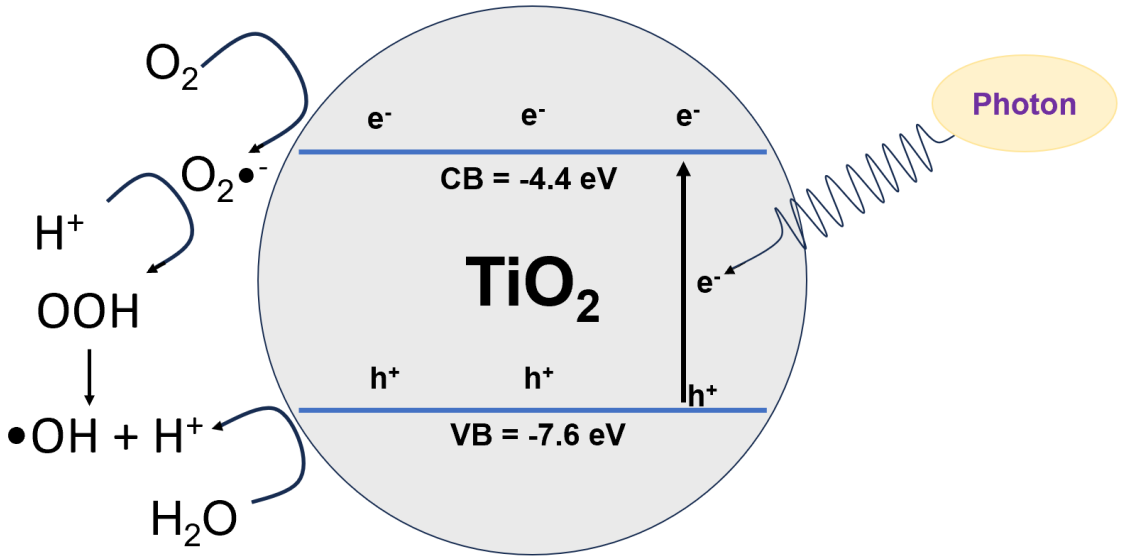

Figure 1.2: Schematic of the Photocatalysis of TiO_2 in the presence of water.

Photocatalyzed TiO_2 will conduct redox reactions with the water at the surface of the material to produce Reactive Oxygen Species (ROSs) in the presence of water. The ROSs include hydroxyl radicals (OH•), and super oxides ($O_2^{\bullet -}$), and other species like H_2O_2 and •OOH. Once the ROSs have been produced, they non-selectively react with organic matter they encounter until they eventually reach termination. Below are the equations of the subsequent redox reaction.

$$TiO_2 + hv \rightarrow e^- + h^+$$

$$e^- + O_2 + H^+ \rightarrow HO_2\bullet$$

$$e^- + HO_2\bullet + H^+ \rightarrow H_2O_2$$

$$2e^- + O_2 + 2H^+ \rightarrow H_2O_2$$

$$h^+ + H_2O \rightarrow \bullet OH + H^+$$

$$2 \bullet OH \rightarrow H_2O_2$$

$$H_2O_2 + hv \rightarrow 2 \bullet OH$$

$$H_2O_2 + e^- + H^+ \rightarrow \bullet OH + H_2O$$

Once the initial redox reactions occur, more photons are required if more redox is desired. Many studies have shown that TiO_2 is effective in breaking down small organic contaminates, textile dyes, and microorganisms in wastewater.[32–35,37–40] This is why many scientists have designed many different TiO_2 nanostructures of various morphologies that are operational under aqueous conditions.

TiO_2 occurs naturally in three allotropic forms rutile, anatase, and brookite, as seen in Figure 1.3. Each of the forms are octahedral TiO_6 unit cells with various distortions, lattices, band gap energies and surface areas. Anatase has a tetrahedral unit square while rutile brookite have octahedral unit squares. [41] Anatase polymorph exhibits a framework of edge-sharing TiO_6 octahedra with an indirect band gap while rutile and brookite consist of both edge and corner sharing configurations with a direct band gap. These polymorphs are commercially available and can also be purchased in mixtures. Degussa TiO_2 is a mixture of anatase and rutile and can be purchased in various ratios of the two crystal structures. Degussa P25 is a mixture ranges from

70:30 to 80:20 anatase:rutile and P90 ranges from 90:10 to 95:5 anatase:rutile.[13,41–43] By mixing anatase and rutile, photocatalytic activity increases significantly. This is why we chose Degussa P25.

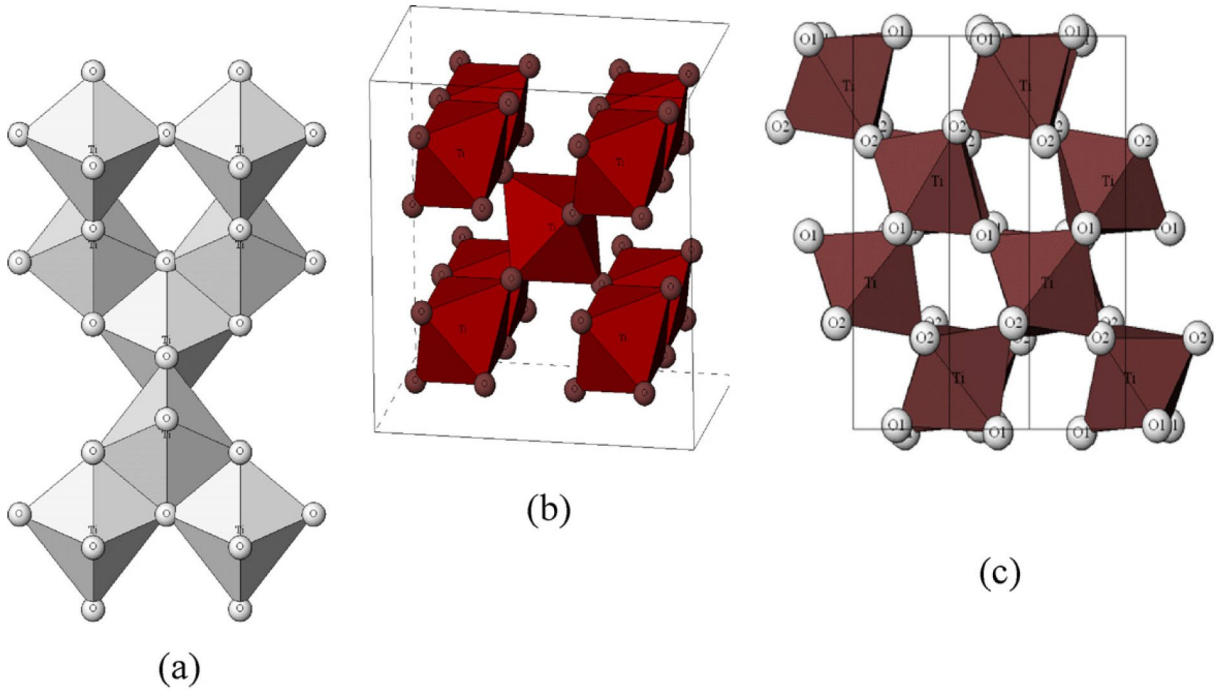

Figure 1.3: TiO_2 crystal structures of the three polymorphs. Image adapted M Pelaez et al.[44]

These differences in activity arise when the Ti-O bond varies. Changes in the Ti-O bonds are significant when examining Raman spectra which reveals tetragonal and monoclinic crystalline phases for anatase and a single monoclinic phase for rutile.[45] Anatase has been shown to have higher photocatalytic activity than the other polymorphs, although scientists are still debating the reason for this. Some hypotheses include larger surface area, lagging charge carrier combination, and higher level of (100) lattice exposure. However, Degussa P25 is consistently shown to be more effective as a photocatalyst than anatase. The scientific community has not been able to demostrate why this is, though they believe that anatase and rutile work in harmony.[46] The assumption is that while anatase is in an activated state, rutile utilizes existing ROSs that would otherwise terminate

redox reactions occurring at the surface of anatase. Another possibility is the charge carriers across the entire photocatalyst is increased by staggered electron-hole pair production.[4748] There is also proposed band gap overlay at the anatase-rutile interface.[49]

1.3 TiO_2 Nanofibers

TiO_2 nanofibers (nanotubes) have been shown to be very diverse in application and so they were chosen as the material for self-assembled membranes. The hydrothermal method was used to create these fibers. During the first 6 h, the nanotubes are formed by the folding and curling of the newly synthesized nanosheets.[21] After 20 h of reaction time, the nanotubes grew in length, about 10 μm with an outer diameter of 12 nm and an interior diameter of 3.7 nm. Figure 1.4 shows an SEM image of the nanotubes after 20 h of synthesis. Figure 1.5 is HRTEM of the nanotubes and their dimensions. [21] These fibers have been successfully vacuum-filtered to form a nanofiber-entangled membrane. Though the membrane was not stable in water, as it broke apart quite easily, it provided an opportunity for dry experiments. Ex-situ TiO_2 experiments are not commonly seen in literature. Yet, they deserve investigation because they allow for smaller scale experimentation, which is beneficial for novel method development.

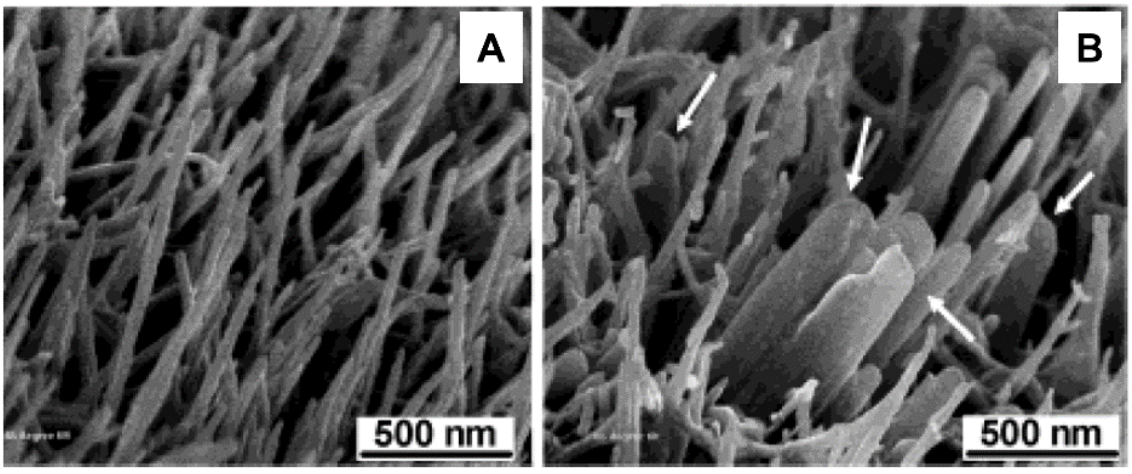

Figure 1.4: SEM Images of nanomaterial after less than 6 h of synthesis. (A) After 6 h. (B) after 3 h. Arrows point to nanosheets folding to form nanotubes. Images adapted from Tian et.al [21]

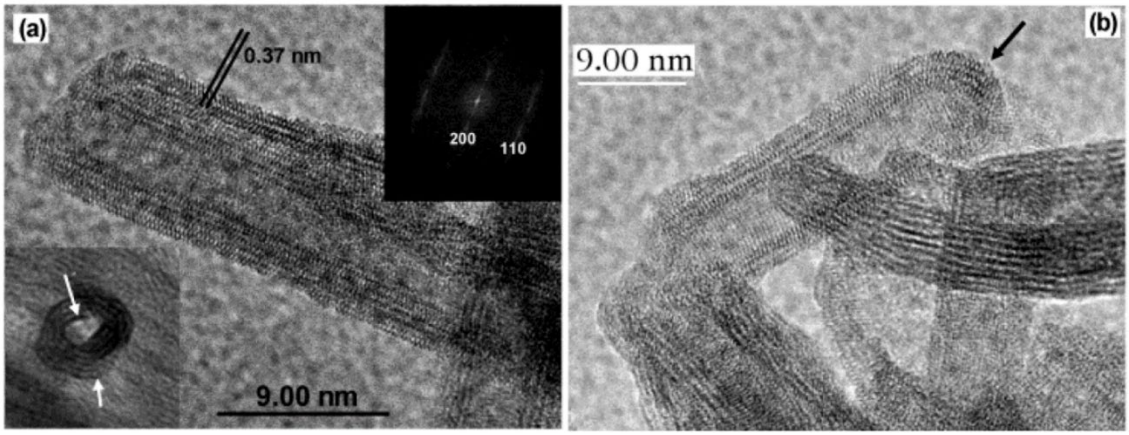

Figure 1.5: (A) An open nanotube. The inset on the left is a cross-section image. The inset on the right is the Fourier transformation of the TEM image. (B) A close-ended nanotube. HRTEM Images adapted from Tian et.al. [21]

1.4.Optimizing TiO_2

Though TiO_2 is widely accepted as an excellent photocatalyst, its high recomination rate causes the semiconductor to have a relatively low efficiency.[50] The activity of TiO_2 also greatly depends on the morphology, heterojunction structure, and crystal structure, orientation, and size of the nanomaterial.[51] These all give reason for augmenting TiO_2. Optimizing these parameters, such as band gap, is incredibly difficult to do, especially in bulk; so, many studies incorporate a material that facilitates photocatalytic activity inot the semiconductive substrate.

It is possible to incorporate metal and nonmetal substances into TiO_2. Nonmetals such as sulfur, nitrogen, and carbon red shift TiO_2 by providing energy levels that fall between the valence band and conduction band. While this provides the photocatalyst with the ability to become more photoactive in the visible range, it has been shown to decrease the optical range of TiO_2. [50] Because the scientific community is searching for new ways to purify wastewater, reducing the optical range is not desirable because sun emits a large spectrum of wavelengths of light. This gives reason to investigate incorporating TiO_2 with metal.

Finding a metal that is easily incorporated into the TiO_2 nanofibers, adjusts the band gap, and provides a higher probability for the formation of charge carriers in sunlight. This is done by incorporating a metal during crystal growth into the structure of the semiconductor, called doping, or by decorating the semiconductor's surface with the metal.[51] Because the nanotubes created by Tian et al an established one-pot hydrothermal method, this study focuses on optimizing the semiconductor by metal-decorating after crystal growth. There were several options of metals to incorporate onto TiO_2. Au, Cu, and Fe are common and well researched; however, Ag was chosen particularly for its antimicrobial capabilities, for its efficiency, and for its well-documented behavior in a multitude of experimental settings.[18,52–55]

Figure 1.6 is a schematic of Ag-incorporated TiO_2 (Ag/TiO_2) reaction to produce ROSs. Because Ag has a Fermi level of -5.5 eV under vacuum, electrons in the valance band of TiO_2 can migrate through the electron orbitals of Ag, thereby shortening the band gap from 3.2 eV to 1.1 eV at the Ag-TiO_2 interface. This allows Ag/TiO_2 to be excited by photons of lower energy at the Ag-TiO_2 interface. [56,57] This increases the ability and efficiency of the photocatalyst as a whole, making it a more suitable photocatalyst for water cleaning under sunlight.

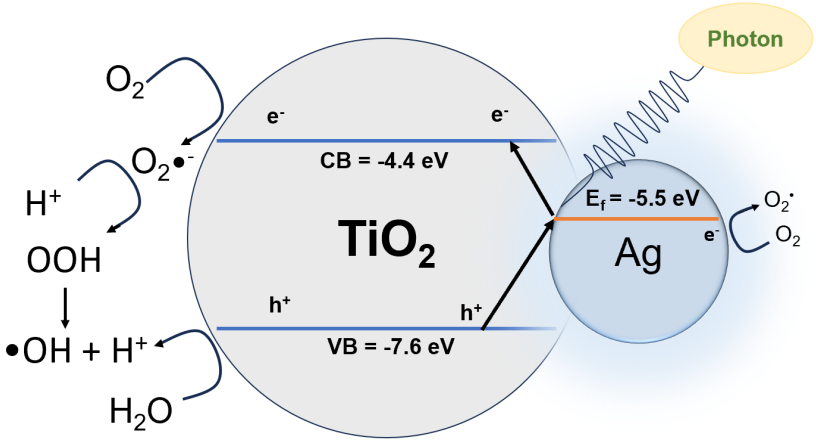

Figure 1.6: Mechanism of Ag/TiO_2 in water to produce ROSs, where E_f is the Fermi level of Ag under vacuum.

1.5. Testing Efficacy by Utilizing Methylene Blue

Because of its popularity, TiO_2 and Ag/TiO_2 have been tested in many ways. Utilizing an aqueous dye is one of the most common methods. Methylene blue is a cationic, organic dye that is used for textiles, cosmetics, art, and staining for medicinal diagnostics.[32,58] It has an absorption coefficient ranging from 4-9 $x10^4$ $M^{-1}cm^{-1}$. As such, it has a very low toxicity and is a popular choice in testing a multitude of semiconductors, especially TiO_2. The dye's brilliant indigo fades as it is broken down by ROSs that are photocatalytically produced. This takes place first by the water molecules adsorbing to the metal oxide's surface at which point dissociation of OH groups take place.[42,59,60] Due to TiO_2's amphoteric nature, we must consider two chemical equilibria. [42]

$$M - OH + H^+ \rightarrow M - OH_2{}^+ \qquad K1 \qquad Eq.1$$

$$M - OH \rightarrow M - O^- + H^+ \qquad K2 \qquad Eq.2$$

Both reactions can take place simultaneously creating an environment ripe for redox reactions. As such, the oxidized methylene blue will gravitate toward the negative site on the semiconductor, where further redox reactions will take place. Studies have shown that an increase in pH causes an increase in the rate of reaction.[42] Ag/TiO_2 is assumed to possess the same proposed mechanism, as seen in the figure below, but operates under a higher wavelength.

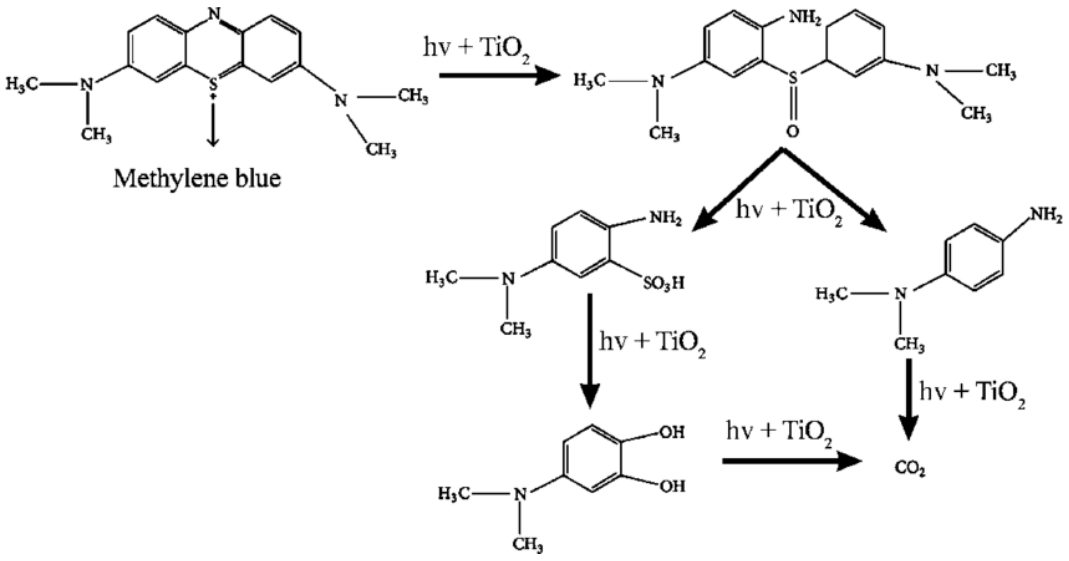

Figure 1.7: Mechanism of Methylene Blue on photoactivated TiO_2. Image adapted from S T T LE et al.[59]

Methylene blue's reaction with air is not as commonly investigated as its reaction with TiO_2, however, studies show there is a dark redox reaction that occurs with air, yielding the formation of *leuco*-methylene blue.[61,62] This is an important aspect to be aware of, because it directly affects the accuracy of all quantitative measurements, in-situ and ex-situ. The mechanism of the dark redox of methylene blue can be seen in the figure below.

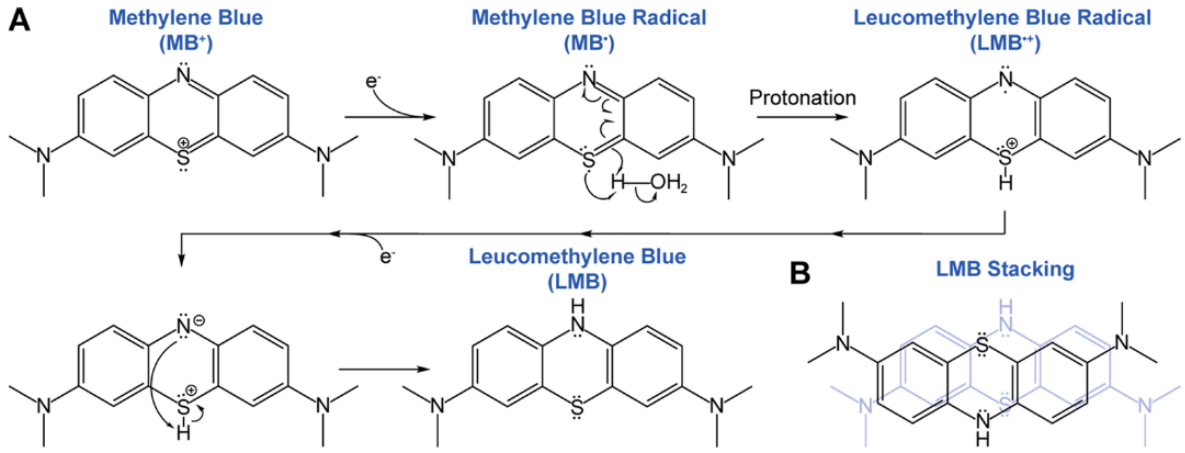

Figure 1.8: Reaction pathway of methylene blue to leuco-methylene blue. A and B indicate the molecules commonly identified in UV-Vis characterization. Image adapted from Mahlum et al.[62]

1.6. Purpose of this Study

Most studies present a method in which a suspension or tablets of TiO_2 are placed in a low concentration of methylene blue under UV light. At various times during the course of the experiment, a specified aliquot of dye is removed from the nanomaterial and taken to a UV-Vis to measure absorbance, or LC/MS and GC/MS if there are multiple species being tested. Systematic errors can be present in this setup. For example, it is possible for methylene blue to react with the air during transport from experimental apparatus to UV-Vis. Other systematic errors exist. Water can evaporate in the experimental apparatus due to an increasing lamp temperature.[63,64] Nanoparticles can remain after centrifuging, causing permanent damage to LC/MS or GC/MS columns. Most solutions to these issues tend to be expensive. Measuring the concentration of the dye and knowing the exact time at which the measurement was taken is nearly impossible. This gives reason to develop a method that takes a picture of the dye that can measure the instantaneous concentration of the dye. The ultimate goal of this study was to develop a method to measure the instantaneous concentration of methylene blue in various dry, photocatalytic environments.

2. Experimental Methods

2.1. Chemicals and Materials

Titanium (IV) oxide nanopowder (≥99.5%, P25 TiO_2 nanoparticles) was purchased from Sigma-Aldrich. Sodium hydroxide (pellet) and sodium borohydride (fine granular, ~99%) were purchased from Macron. Silver nitrate (99.9995%) was purchased from Alfa Aesar (Premion in Ward Hill, MA). Methylene blue powder was purchased from TCI. All experiments used 18Ω H_2O.

2.2. Materials Preparation

2.2.1. TiO_2 Nanofiber Synthesis

The TiO_2 nanofibers were synthesized using the hydrothermal method.[21] To begin, 40 mL of 10 M NaOH was prepared and added to a 50 mL Teflon vessel. Next, 500 mg (or 1000 mg) of P25 TiO_2 nanoparticles was added and stirred into the solution. The Teflon vessel was placed in a 100 mL Baoshishan hydrothermal synthesis reactor. The reactor was left in a VWR Shel Lab oven (Model No. 1350FM, 13.0 A, 115 V, 80 Hz) at 220°C for five days. Following this, the reactor was taken out of the oven and left to cool in a fume hood at room temperature for approximately 12 h. The nanofiber product precipitated at the bottom of the reaction. After the supernatant was decanted, the product was redispersed in 300 mL of water and transferred to a beaker. The resulting aqueous nanofiber dispersion was transferred to centrifuge tubes and centrifuged (Eppendorf Centrifuge 5804) at 9000 rpm for 10 min. The pH of the supernatant was checked using MicroEssential pH paper before decanting, and the product was redispersed in water. This purification process was repeated until the pH reaches neutral. The resulting nanofiber product was then dried in an oven at 45 – 60 °C for 24 h.[22,26,43] Though the nanofibers were thoroughly sonicated and vortexed, there were still dense aggregates that went unnoticed. It is possible that the surviving aggregates encapsulated hydroxide.

2.2.2. TiO_2 Self-Assembled Membrane Fabrication

Roughly 300 mg of the nanofiber product obtained from the previous synthesis was suspended in 40 mL of water, the aggregates were then successfully broken apart and suspended. The mixture was transferred to a vacuum filtration system. Once dried, the membrane formed on the filter was removed from the system, placed on a glass plate, and flattened by applying pressure with a large beaker. The membrane was dried in a 45-60 °C oven.

2.2.3. Preparation of a 5% Ag-Incorporated (Ag/TiO_2) Membrane

First, 290 mg of the nanofiber product was prepared in a 50 mL centrifuge tube and suspended in approximately 50 mL of water by sonication. Next, 23.0 mg of $AgNO_3$ was then added to the suspension and the centrifuge tube was sonicated to allow $AgNO_3$ to dissolve. Following this, 51.0 mg of $NaBH_4$ was added to the suspension. The suspension was then vortexed and aspirated by opening the cap of the centrifuge tube. The contents of the centrifuge tube were sonicated for 3 min and aspirated every 30 s. The suspension was vacuum filtered into the TiO_2 nanofiber membrane and dried completely in an oven at 45-60 °C as described previously.

2.3.Materials Characterization

The XRD patterns of the samples (i.e., commercially available P25 nanoparticles, synthesized TiO_2 nanofibers and Ag/TiO_2 nanofibers) were recorded using an X-ray diffractometer (**Rigaku XtaLAB Synergy-S diffractometer).** Each sample was put on the nylon loop and scanned using CuKα (0.04 W, 30 kV, and 15 mA) from angles from 10 to 130 degrees at a speed of 1.000 degree. The UV-Vis spectra of the samples suspended in water and dye aqueous solution were taken using a UV-Vis spectrometer (Agilent Cary 60). The FTIR spectra of the solid samples were obtained in attenuated total reflection (ATR) mode with 64 scans by the FTIR spectrometer (IRAffinity-1S Shimadzu).

2.4. Dye Degradation on Photocatalytic Membranes using a Gel Imaging System

All Gel Imaging System experiments occurred within a 4 week period. The calibration curve of methylene blue on the membranes was obtained by drop-casting 10 µL of 0 ng, 7.5 ng, 36.3 ng, 49.6 ng, 72.3 ng methylene blue onto the membrane. A grey scale image of the membrane was taken on parafilm in the UVP ChemStudio touch (Analytik Jena Imager) under colony count setting with 50 ms exposure time. The intensity of each dye dot was analyzed by Image J.

The dye degradation experiments were conducted in four photocatalytic environments—TiO_2 Dark, TiO_2 Light, Ag/TiO_2 Dark, and Ag/TiO_2 Light. For the dark experiment, images were taken every 0.5 or 1 min for 5 min using 50 ms exposure time for TiO_2 membrane and 150 ms exposure time for Ag/TiO_2 membrane, respectively. For the light experiments, the Xe lamp was on at all times during the 5 min experiment. Specifications for all four experimental conditions are in Appendix B. The same two membranes were used for all experiments, one TiO_2 membrane and one Ag/TiO_2 membrane. All dye droplets were taken from the same two stock solutions. The stock solutions were taken to the UV-Vis in order to calculate the exact mass in each 10 μL dye droplet.

2.5. Analysis of Dye Intensity on Photocatalytic Membranes using ImageJ

Each image was cropped to contain only the membrane without any background. The contrast of each image was inverted such as the dye dots were displayed in gray. The mean grey value (Mean GV) of the membrane background was measured by utilizing the oval brush. The Mean GV for each dye dot (i.e., 0 ng, 7.5 ng, 36.3 ng, 49.6 ng, 72.3 ng of methylene blue) was measured using the polygon selection to isolate them from the background. The Mean GV is equal to the sum of all gray values of all pixels in the selected area divided by the number of pixels.[65] The intensity was calculated by Equation 3 where the GV_s and GV_b are the Mean Grey values of the sample and background and $Area_s$ and $Area_b$ are the areas of the sample and background droplets, respectively.

$$Intensity = GV_s \times Area_s - GV_b \times Area_b \qquad Eq.3$$

3 Results and Discussion

3.1 Materials Characterization

Figure 3.1 displays images of the TiO_2 and Ag/TiO_2 membranes. The surface of the TiO_2 membrane was quite smooth and dull while the Ag/TiO_2 membrane's surface possessed a rough

texture and was shiny. Ideally, the textures would be almost identical, however, during the process of reducing the silver, the texture changed. Hydrogen gas was released as result of $NaBH_4$ reducing the silver onto the TiO_2 fiber in situ. After approximately 30 min, and the fabrication began. During vacuum filtration, very small bubbles formed at the surface of the fibers. This indicated there was a minute amount of unreacted $NaBH_4$ that was forming H_2 gas. These bubbles left small craters in the membrane's surface. The pH of each membrane was tested using pH paper and were found to be basic. While the supernatants of neutralization process were neutral after processing and before membrane fabrication, the redispersion of TiO_2 fibers had a pH of approximately 10 and Ag/TiO_2 a pH of approximately 9. This basicity indicates OH^- groups were entrapped among the fibers or remained on the surface of fibers due to the presence of very small aggregates of TiO_2 fiber. These fibers withstood sonication in bulk yet broke down in pre-fabrication sonication which contained residual OH^-.

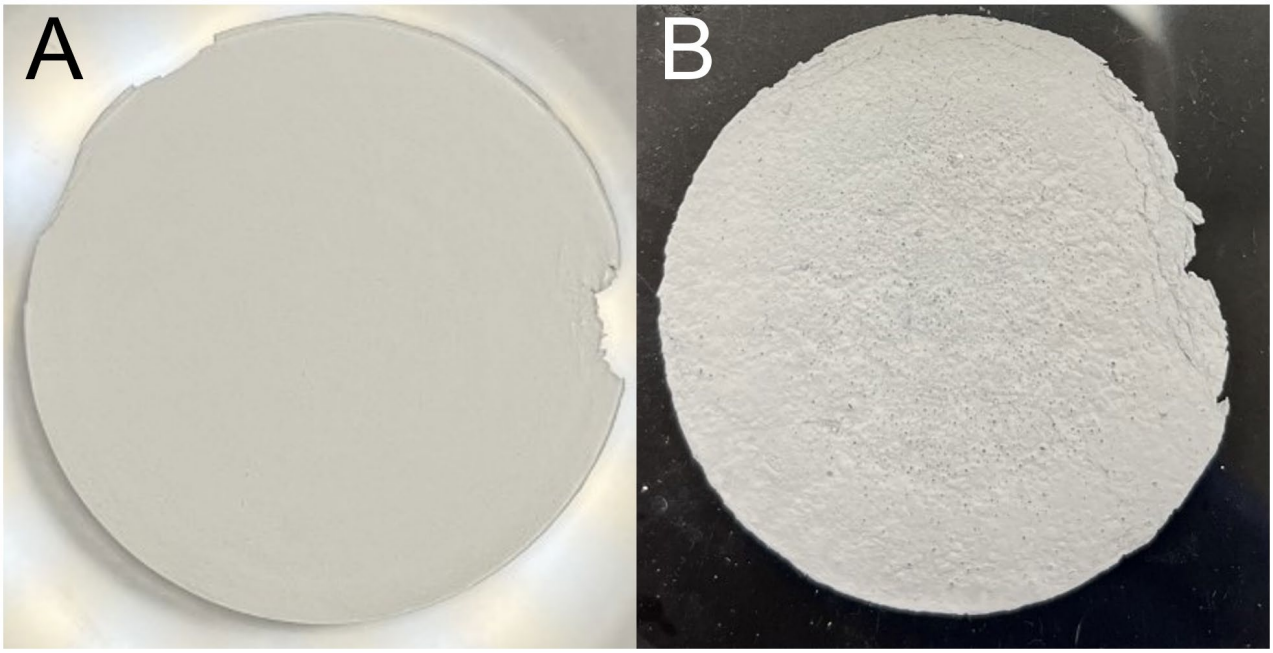

Figure 3.1: (A) TiO_2 nanofiber membrane (B) Ag/TiO_2 nanofiber membrane.

XRD was used to confirm the structures of the materials. Figure 3.2 shows the XRD patterns of the TiO_2 nanofibers (black), Ag/TiO_2 fibers (red), and the Ag particles (blue). For the TiO_2, peaks were found at 25.13, 29.53, 35.27, 38.43, 48.53, 52.43 and 60.74 degrees that correspond to indices of (101), (004), (001), (200), and (204) of anatase, respectively;[66,67] and peaks were found at 29.53, 34.34, and 52.43 degrees that correspond to indices of (110), (101), and (211) of rutile, respectively.[68–71] The XRD pattern for TiO_2 and Ag/TiO_2 membranes were found to be similar. The XRD pattern for Ag particles showed high crystallinity and a nearly identical pattern to literature values with indices (111), (200), (220), (311), (222), (400), (331), and (400) at 38.15, 44.34, 64.47, 77.44, 81.59, 110.60, and 115.01 degrees.[67]

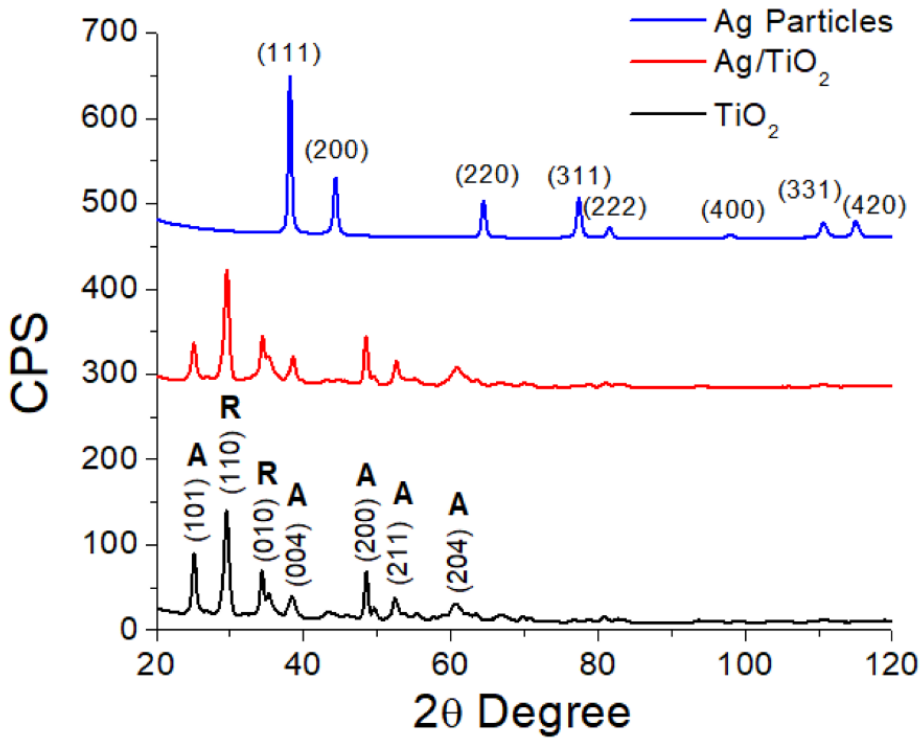

Figure 3.2: XRD overlay of nanomaterials with all associated indices and crystal structures. Anatase was labeled "A", rutile was labeled "R", and Ag particles were labeled "Ag."

Compared to the Ag particles, the XRD pattern of Ag/TiO_2 does not contain metallic Ag. However, the Ag/TiO_2 nanofiber sample does appear slightly different from the TiO_2 nanofiber sample as shown in Figure 3.2. Therefore, further analysis took place. Because the synthesis of Ag occurred under the basic conditions, it is likely that Ag_2O and AgOH formed instead of Ag in the Ag/TiO_2 sample following Equations 4 and 5.

$$NaOH_{(aq)} + AgNO_3 \rightarrow NaNO_{3\,(aq)} + Ag_2O + H_2O \qquad Eq.4$$

$$NaOH_{(aq)} + AgNO_3 \rightarrow NaNO_{3\,(aq)} + AgOH \qquad Eq.5$$

To confirm this, a closer look at the Ag/TiO_2 sample, an additional set of peaks at 27.92, 32.23, and 53.61 degrees that would be assigned to Ag_2O (110), (111), and (211) indices, respectively. Ag_2O does not seem to appear in the XRD pattern as indicated in Figure 3.3. [4,5,7] Due to amorphous nature of AgOH, it is difficult to obtain it XRD pattern. It also cannot be ruled out that the content of Ag might be lower than the detection limit (< 10%) of the XRD. Because of the difference in the appearance of Ag/TiO_2 membrane and its experimental behavior (as it will be discussed in later sections) as compared to TiO_2 membrane, it is most likely that oxidized Ag incorporated to the membrane. Further ICP/MS analysis might be able to resolve the Ag content in the membrane. While the presence of the Ag particles, whether Ag_2O or AgOH, was not identified in XRD, experimental results from TiO_2 and Ag/TiO_2 membranes are significantly different. Therefore, it is most likely that the oxidized Ag content was below the detection limit, or that the Ag content was mostly amorphous.

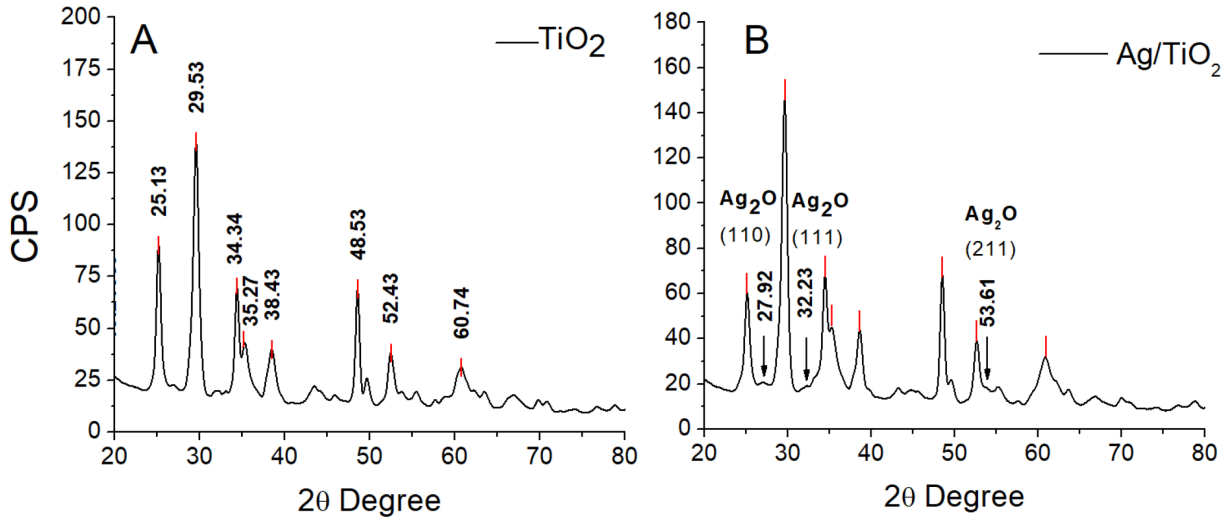

Figure 3.3: XRD of (A) TiO_2 membrane with associated angles and (B) Ag/TiO_2 membrane with associated angles and indices.

UV-Vis spectra were acquired for the TiO_2 and Ag/TiO_2 nanofiber suspensions in aqueous solution respectively, as shown in Figure 3.4. The concentrations of the suspensions were not considered for the samples as the purpose of this characterization was qualitative rather than quantitative. The TiO_2 aqueous suspension exhibited a broad peak at 288 nm. The literature report that most of the spectra for TiO_2 nanofibers showed the major peak with a range of 280-330 nm compared to that of TiO_2 P25 nanoparticles with a peak residing at roughly 325 nm.[23,2472] This difference in literature values exists simply because spectra can greatly vary from study to study. Depending on the fabrication method, it is possible for a particular facet or a TiO_2 phase more interactive with light at lower wavelengths to be located at the surface of the material.[16,23,73] Some authors have proposed the in-plane interactions of the anatase (001) lattice are stronger than those that are perpendicular to it. Although anatase preferentially expose (100), (101), and (001) surfaces, it is possible those will become covered by other phases of TiO_2, such as rutile, whose interfaces are less interactive with photons of a low wavelength.[74] The Ag/TiO_2 nanofiber aqueous

suspension showed a nearly identical spectrum. It is expected to see a peak at 400-420 nm if significant amount of metallic Ag particles is incorporated to the TiO_2 nanofiber,[66,70,75] but it was not observed. This result suggests that the metallic Ag nanoparticles are not present.

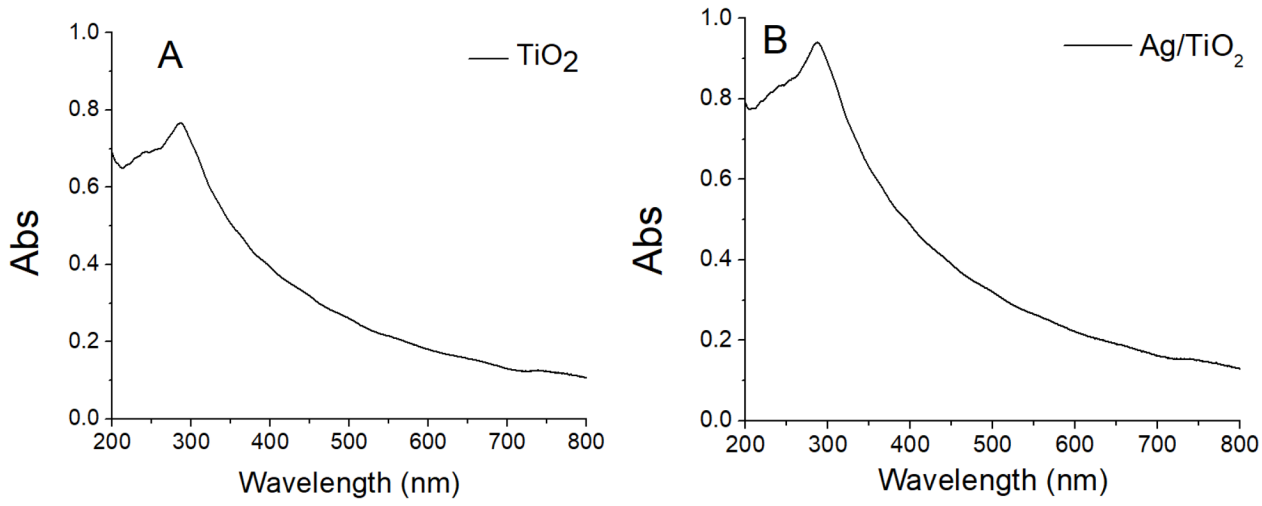

Figure 3.4: UV-Visible spectra of TiO_2 nanofiber aqueous suspension (A) and Ag/TiO_2 nanofiber aqueous suspension (B). Note that they are not the same concentration.

To further investigate the presence of Ag content in the membrane, a Tauc plot was constructed to measure the band gap. The Tauc plot method utilizes Equation 6,

$$(\alpha \cdot h\upsilon)^{1/\gamma} = B\left(h\upsilon - E_g\right) \qquad Eq.6$$

Where the energy-dependent absorption coefficient is a, h is plank's constant, v is the photons frequency, E_g is the band gap energy, and B is a constant. An important note to make is the γ factor—γ refers to the direct or indirect transition in the band gap (1/2 or 2 respectively).[20] Because Degussa P25 has both direct and indirect band gaps, many studies have shown that the mixture of anatase and rutile exhibit direct band gap behavior. While the photocatalytic material used in this study was consistent with this phenomenon, a Tauc plot for indirect band gap was examined for this study and can be found in the Appendix. The Tauc plot for a direct band gap revealed TiO_2 to

have a band gap of 3.44 eV and Ag/TiO_2 with 3.38 eV. These values are larger than what the literature values are (TiO_2, 3.2 eV; Ag/TiO_2, 2.5 eV).[51,55,66,67,72] The most probable reason for the discrepancy is that there is a small amount of quantum confinement present in the TiO_2 fiber. Quantum confinement can occur when the e-/h+ pair's energy levels are too close together. This causes band gap expansion and is the most likely explanation for the larger than normal value for both TiO_2 and Ag/TiO_2. The high band gap of the Ag/TiO_2 is most likely due to the small size of the Ag particles (Ag_2O and AgOH) that do not cover a larger surface area of TiO_2. Therefore, there are fewer Ag-assisted excitations as compared to TiO_2 excitations. [17,18]

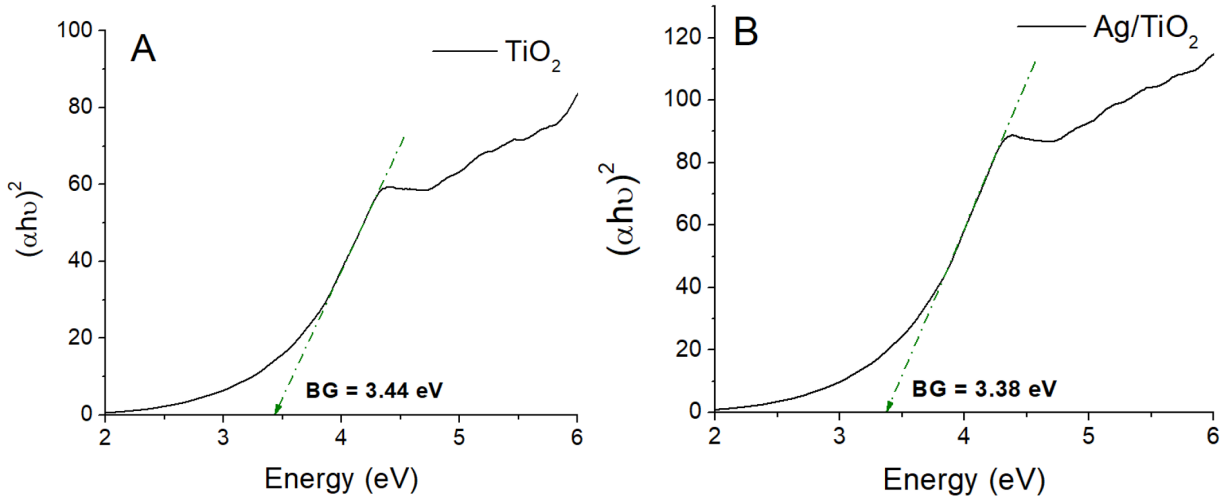

Figure 3.5: Tauc plots for (A) TiO_2 and (B) Ag/TiO_2 membranes were plotted to measure the direct band gap of each semiconductor.

There are several reasons the spectra look similar. The first being that the Ag particles failed to deposit onto the membrane. There were differences in the membranes' appearances; TiO_2 membrane was a bright, white color and the Ag/TiO_2 membrane was a shiny, silver color. The second possibility was that the concentration of Ag content that was successfully deposited was so low that the TiO_2 peak shielded the red shift. A third possibility was that $AgNO_3$ was not finished

reacting with $NaBH_4$. If this were the case, residual $NaBH_4$ could still exist in the suspension. A series of characterizations were conducted to investigate this further. [1,2,19–23]

An IR spectrum was taken of each of the materials to find and identify the presence of organic contaminates (Figures 3.6 and 3.7). The sample preparation involved taking small portions of new TiO_2 and Ag/TiO_2 membranes The IR spectra for TiO_2 and Ag/TiO_2 membranes showed a large broad peak at roughly 3100 cm^{-1}. This peak is commonly associated with an O-H stretch and in this case is most likely due to the presence of OH^-.[76] Both membranes contain peaks in the fingerprint region that are characteristic of TiO_2 (900 cm^{-1}, 760 cm^{-1}, and 685 cm^{-1}). A weak, yet broad peak at approximately 1650 cm^{-1} was found in both membranes. While $NaBH_4$ has a peak at 1620 cm^{-1}, it is sharp.[77] $NaBH_4$ does not appear to be present in the membranes.

While it is unlikely that metallic Ag formed in situ, a closer look at the biproducts of the reduction of Ag under FTIR spectroscopy. Equations 7-9 shows the possible reactions under examination.

$$2AgNO_3 + 2NaBH_{4\,(aq)} \rightarrow 2Ag_{(s)} + B_2H_6 + H_{2\,(g)} + 2NaNO_3 \qquad Eq.7$$

$$B_2H_6 + 6H_2O \rightarrow B(OH)_3 + 6H_2 \qquad Eq.8$$

$$2AgNO_3 + H_2 \rightarrow 2Ag + 2HNO_3 \qquad Eq.9$$

$NaNO_3$ possesses a strong, broad peak that ranges from 1680-1420 cm^-.[77] While a weak, small yet broad peak at 1657 was found in both membranes, further testing would need to be done to confirm the presence of $NaNO_3$. FTIR spectra for TiO_2, $NaBH_4$, and $NaNO_3$ from SDBS was used as comparison and can be found int the Appendix.

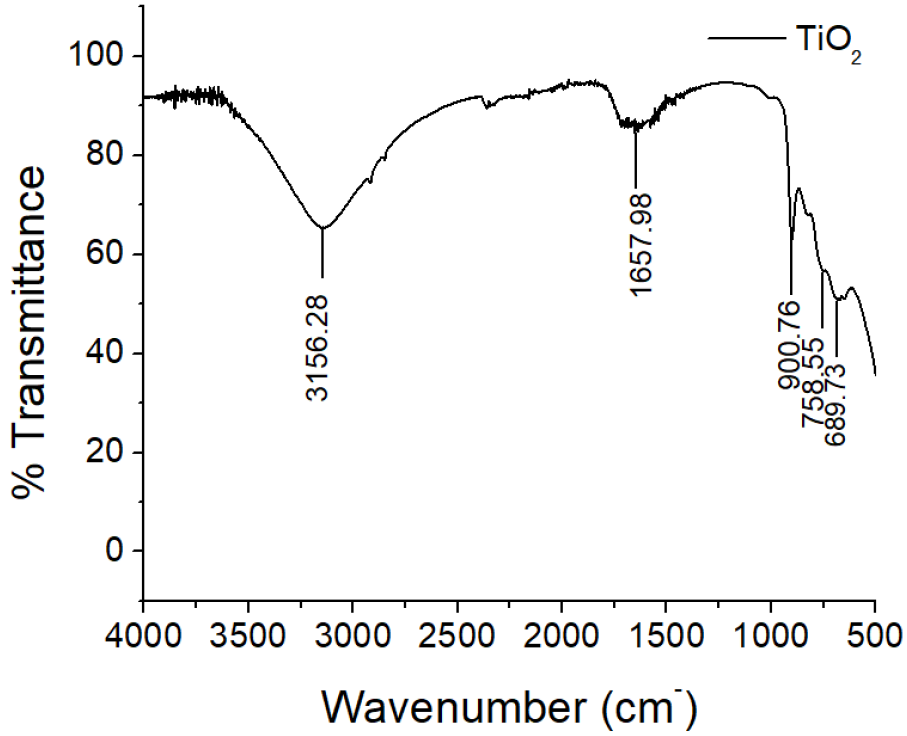

Figure 3.6: FTIR of dry TiO_2 membrane

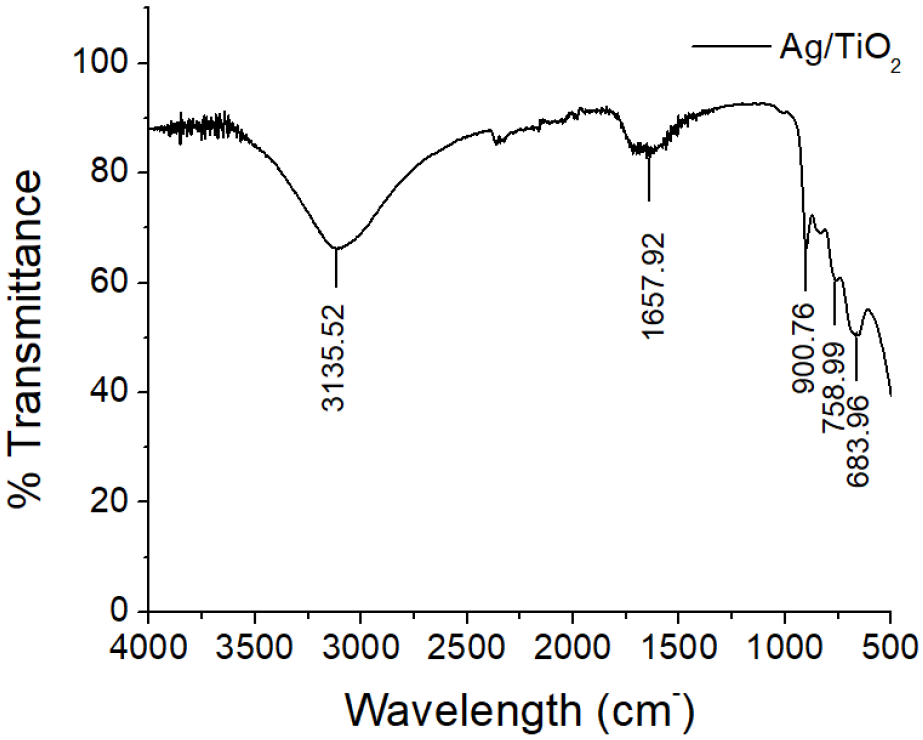

Figure 3.7: FTIR of dry Ag/TiO_2 membrane

3.2 Dye Calibration

A UV-Vis spectrum (Figure 3.8) was obtained for the following concentrations of methylene blue: 3.13 $\times 10^{-6}$ M, 7.82 $\times 10^{-6}$ M, 9.38 $\times 10^{-6}$ M, 12.5 $\times 10^{-6}$ M, 18.8 $\times 10^{-6}$ M, 25.0 $\times 10^{-6}$ M, and 31.3 $\times 10^{-6}$ M. The solutions were made by creating a 3.13 $\times 10^{-4}$ M solution and then diluting to the appropriate concentrations. The λ_{max} was 665 nm for all concentrations and is characteristic of the dye.[34] The spectrum was characteristic of a methylene blue at room temperature and as such, the absorption coefficient of the dye was 5.22 $\times 10^{4}$ $M^{-1}cm^{-1}$.[40,58,61,62] Due to its proclivity of redox in the presence of air even in dark conditions, this calibration curve (Figure 3.9) was created with fresh samples.

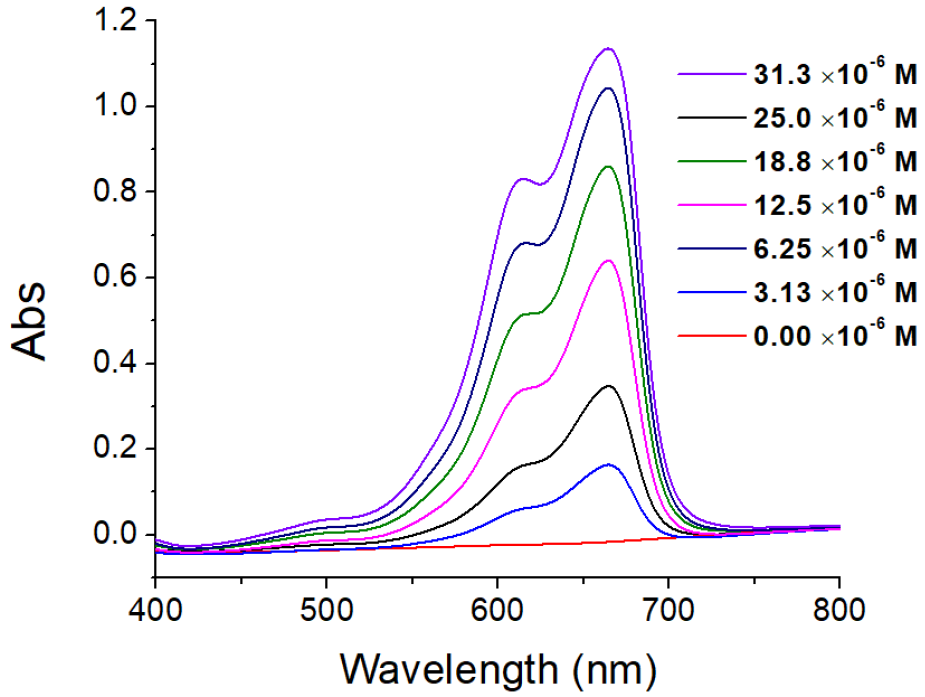

Figure 3.8: UV-Visible spectra of methylene blue (MB) taken in November 2023. Molar concentrations 3.13 $\times 10^{-6}$ M, 7.82 $\times 10^{-6}$ M, 9.38 $\times 10^{-6}$ M, 12.5 $\times 10^{-6}$ M, 18.8 $\times 10^{-6}$ M, 25.0 $\times 10^{-6}$ M, and 31.3 $\times 10^{-6}$ M correspond to 0.0 µg, 2.0 µg, 5.0 µg, 6.0 µg, 8.0 µg, 12.0 µg, 16.0 µg, 20.0 µg in 2 mL of water.

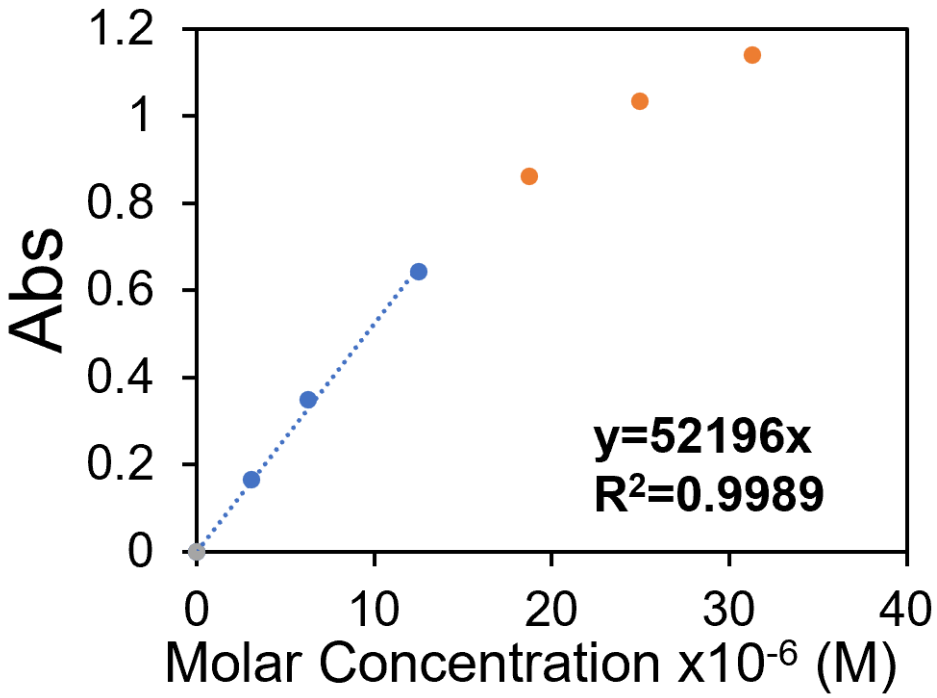

Figure 3.9: Methylene blue calibration curve from the UV-Vis spectrum in Figure 3.8.

Immediately after all Gel Imaging System experiments had been conducted, the dye samples' absorbances were measured to ensure accuracy for all subsequent kinetic information. Figure 3.10 shows the spectra for all experimental samples of dye. The absorbances at λ_{max} were divided by the absorption coefficient to yield the mass of the dye in the 10 µL dye droplets used for the experiments. Table 3.1 shows the absorbance of the 2 mL experimental samples, their associated molar concentrations, and the mass of methylene blue in each of the 10 µL droplets.

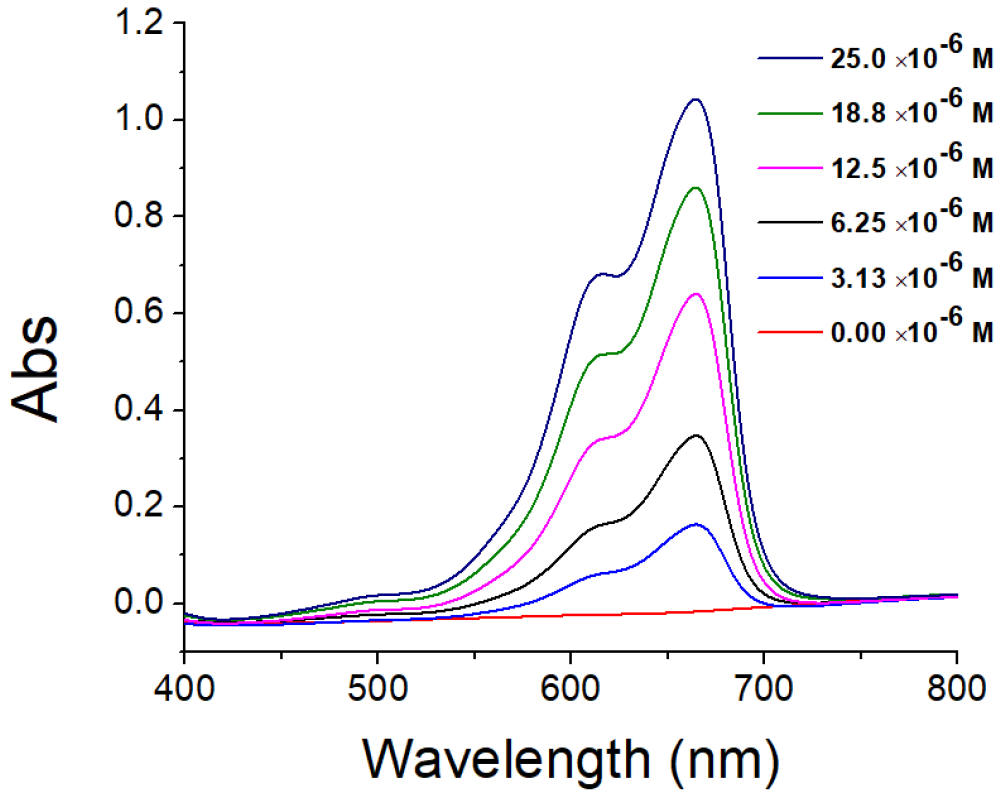

Figure 3.10: UV-Vis spectra of methylene blue samples that were used in all Gel Imaging System experiments and their corresponding molar concentrations.

Table 3.1: Table of experimental molar concentrations and masses in 10 µL droplets and their corresponding absorbances.

Absorbance	Molar Concentration	Mass of 10 µL Droplet
0	0.00 ×10^{-6} M	0.0 ng
0.123	2.76 ×10^{-6} M	7.5 ng
0.593	13.3 ×10^{-6} M	36.3 ng
0.81	18.2 ×10^{-6} M	49.6 ng
1.18	26.5 ×10^{-6} M	72.3 ng

3.3 Digital Dye Quantification by Gel imaging System and ImageJ

3.3.1 Calibration Curves for Different Conditions

The goal for collecting a calibration curve was to isolate the linear range of the dye drop cast to the membrane according to Beer's Law and to quantify the mass of methylene blue versus the color intensity of the dye on the photocatalytic membranes of each experiment. Each sample circle was formed by drop casting 10 μL of the solutions listed in Table 3.1, resulting in corresponding sample mass in the circle. Figure 3.11 is the image from which the calibration curve was analyzed. For droplets of higher concentration, the calibration curve experienced a dramatic curvature. This curvature is historically seen in oversaturated spectroscopic spectra like highly concentrated UV-Vis samples. The higher concentrations were not included in the methylene blue calibration curve because they did not fall into the linear region according to Beer's law. In the case of overly concentrated UV-Vis samples, diluting highly concentrated samples remedy the oversaturation.

The first observation to be discussed is the uneven nature of dye distribution on the substrate. In the droplets with higher concentrations, this phenomenon is more evident and can be seen most prominently in the 36.3 ng, 49.6 ng, and 72.3 ng samples.

The second observation that can be made is the droplet size and shape. Though each sample was 10 μL, they were never perfectly spherical or uniform. The size of the droplets also changed over time. Though this is not directly related to the calibration curve, it is worth mentioning because it is another reason for manually outlining the droplet. Automatic trancing would, at time, ignore small amounts of dye that can be seen with the naked eye. Choosing to manually tracing each circle to ensure the complete coverage before quantifying the Mean GV. This adaptation ensures a more precise and accurate reading of the color intensity for all samples.

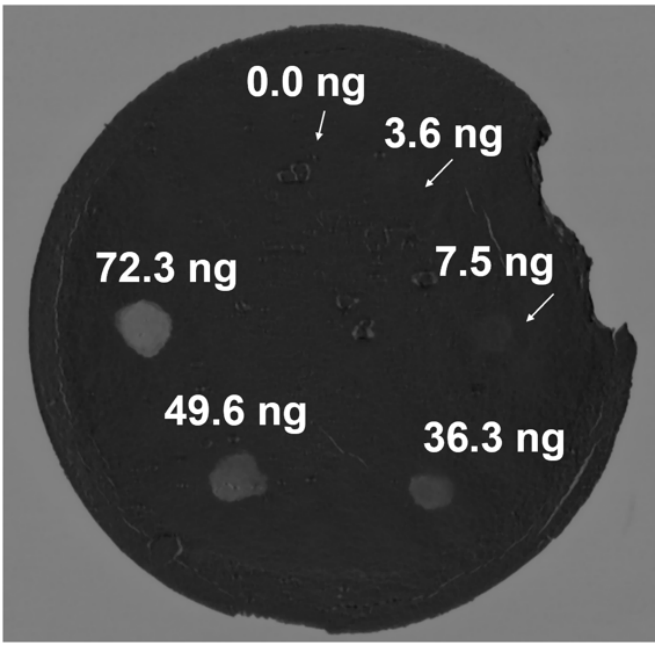

Figure 3.11: Image of Calibration Curve for MB on TiO_2 membrane in a dark experiment. The masses are listed above the droplets with arrows identifying the location of droplets that are difficult to see.

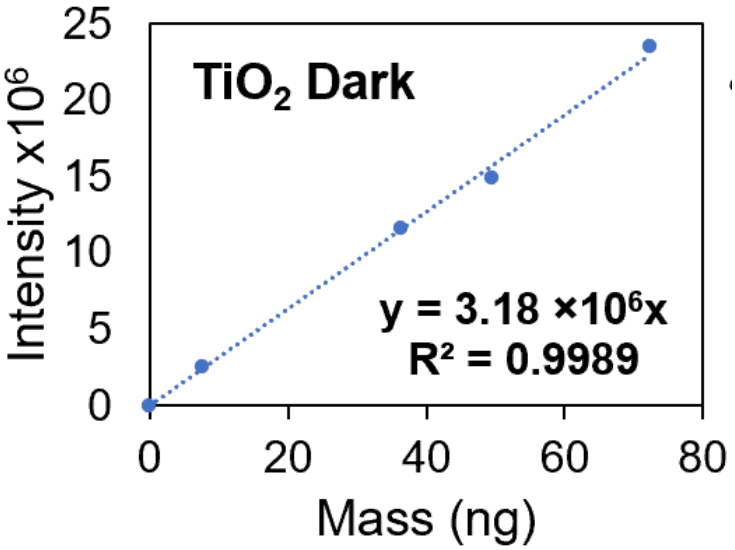

Figure 3.12: Calibration Curve for TiO_2 Dark. A) Calibration curve from 0 to 49.6 ng. B) This calibration curve was constructed by setting the x-intercept to 0.

Figures 3.13, 3.14, and 3.15 are the collection of the calibration curves for TiO_2 membrane in the light, and Ag/TiO_2 membranes in the dark and the light. The linear regression equations for each are very similar. With intercepts set to zero, sensitivities, which are the slopes, were found to be in the same magnitude and R^2 values above 0.98. For each graph, the intensity is linearly proportional to their respective mass across the four various environments. However, the slope is different. The cause for this was most likely due to the uneven nature of the dye spreading across the membrane surface. Although the same methylene blue solutions were used for all calibration curves and experiments, the sensitivity was greatly affected by the deposition of the droplet on the substrate. Evenly depositing 10 µL proved to be quite a challenge. Any change in the pipet's angle, deposition speed, or shaking would affect the droplets' size, shape, and uniformity. Despite these shortcomings, calibration curves were consistently collected with R^2 values of ≥ 0.9820 with the digital quantification in ImageJ. Therefore, the linear region was identified and can be used for quantifying the disappearance of the methylene blue at a fixed mass in this region due to degradation in the kinetics experiments.

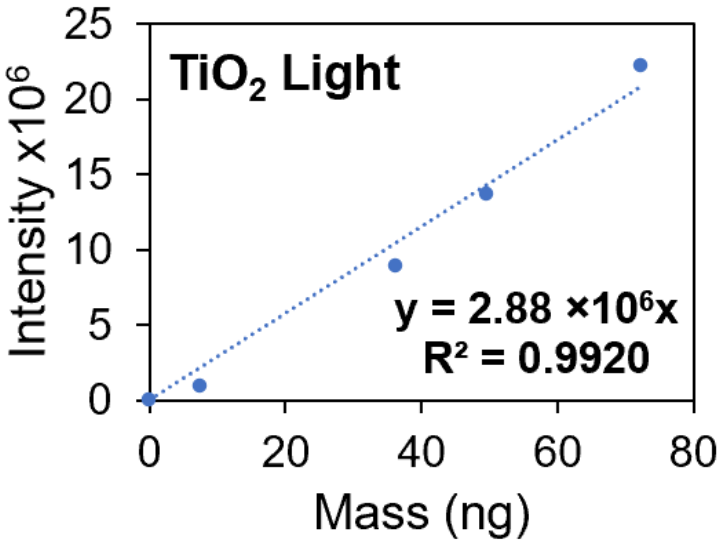

Figure 3.13: Calibration curve for methylene blue for the TiO_2 light experiment.

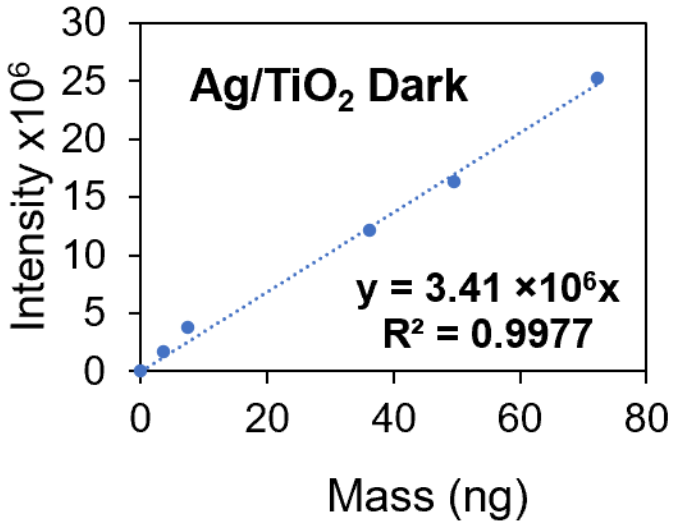

Figure 3.14: Calibration curve of methylene blue for the Ag/TiO_2 dark experiment

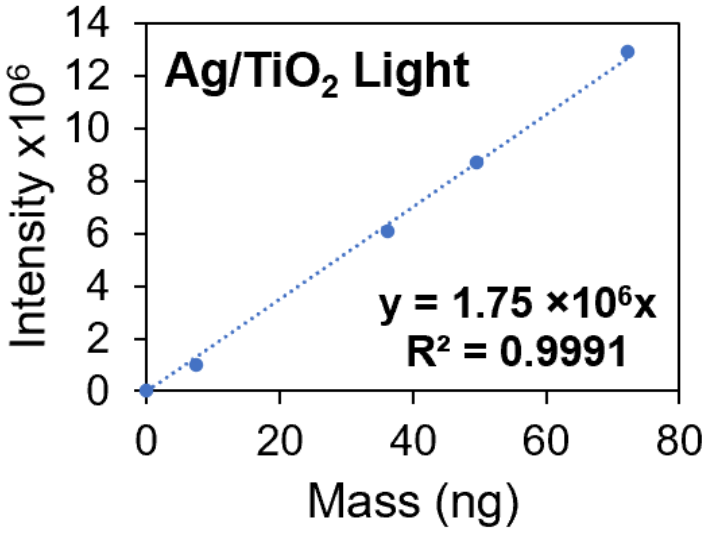

Figure 3.15: Calibration curve of methylene blue for the Ag/TiO_2 light experiment

Subsequent calibration curves were collected to determine the reproducibility of this method. Droplet masses that exceeded 72.3 ng did not fall within the linear region for any experimental conditions. A dramatic curvature was seen in the graph (as seen in Appendix, Figure A2). The hypothesis was that it would be possible to use the calibration curve seen in Figure 3.12-

3.15 for all of their respective experimental conditions. This was not the case. While this method was able to render calibration curves with R^2 values of 0.9820 and higher for each experiment, the slopes varied. Because the slopes varied from experiment to experiment, the calculated methylene blue mass inaccurate. This demonstrated that the calibration curves in Figures 3.12-3.15 were not suitable to accurately calculate dye mass. In response, new calibration curves were made for each experiment and used to calculate to dye masses. This yielded the data found below. All averaged initial masses fell within ±3 ng of the true mass.

Table 3.2: All initial masses (M_i) of dye droplets in this study.

TiO_2 Dark			
36.3 ng droplet		49.6 ng droplet	
Date	M_i	Date	M_i
1	36.5	1	49.5
2	38.0	2	47.5
3	37.9	3	44.4
Ave	**37.5**	**Ave**	**47.1**
Std Dev	**0.68**	**Std Dev**	**2.10**

Ag/TiO_2 Dark			
36.3 ng droplet		49.6 ng droplet	
Date	M_i	Date	M_i
1	38.4	1	46.2
2	31.6	2	42.1
3	48.5	3	51.7
Ave	**39.5**	**Ave**	**46.7**
Std Dev	**6.94**	**Std Dev**	**3.93**

TiO_2 Light			
36.3 ng droplet		49.6 ng droplet	
Date	M_i	Date	M_i
1	39.7	1	49.3
2	30.9	2	47.3
3	37.7	3	56.9
Ave	**36.1**	**Ave**	**51.2**
Std Dev	**3.77**	**Std Dev**	**4.14**

Ag/TiO_2 Light			
36.3 ng droplet		49.6 ng droplet	
Date	M_i	Date	M_i
1	41.8	1	49.7
2	30.9	2	47.3
3	35.3	3	56.7
Ave	**36.0**	**Ave**	**51.2**
Std Dev	**4.48**	**Std Dev**	**3.99**

3.3.2 Methylene Blue Dye Degradation

3.3.2.1 Degradation of Dye on the Membranes under Different Conditions

The purpose of this analysis was to study the degradation of methylene blue dye under different conditions. The specifications of the four different conditions and calculated initial masses can be found in the Appendix B. The hypothesis was that TiO_2 Dark Experiments would

yield the smallest percentages while Ag/TiO_2 Light Experiments would yield the highest degradation percentages. Figure 3.18 is a time lapse of a TiO_2 Dark Experiment and an example of a typical degradation experiment. As can be seen, a significant amount of dye was broken down in droplets of lower concentrations. The 7.5 ng droplet is very hard to identify but can still be seen and measured in ImageJ after the inversion for 0 min image. However, it was nearly impossible to make out the edges of the droplet after 1 min and therefore has been removed from all data analyses. Figure 3.19 is a graph of the mass degradation over time for a TiO_2 dark experiment. Compared to the control experiment on the filter paper that is made of cellulose (found in Appendix A), the dye was degraded faster on the TiO_2 surface in dark.

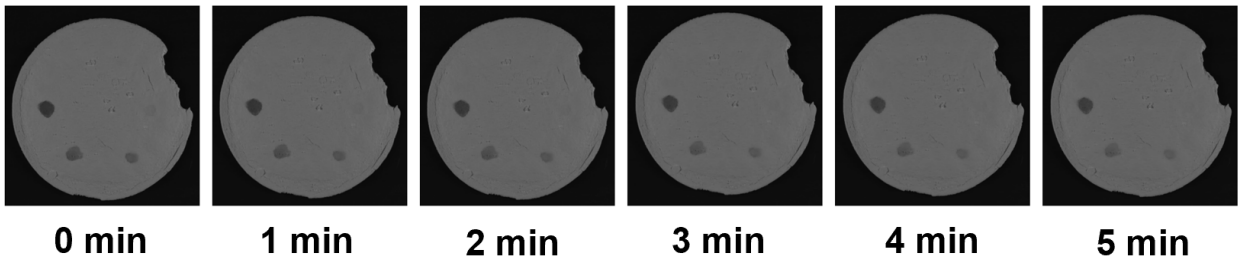

Figure 3.18: Unedited image of typical degradation experiment. This is a time laspe of a TiO_2 dark experiment.

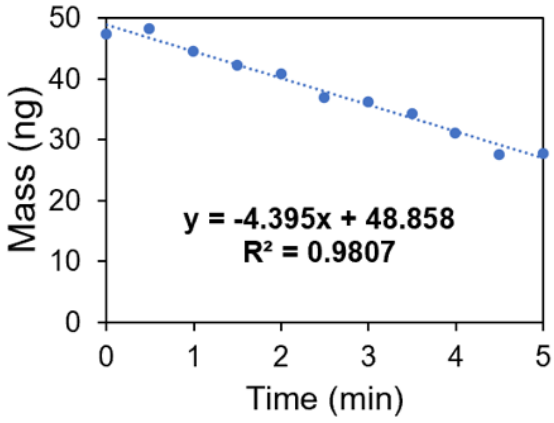

Figure 3.19: Methylene blue breakdown over time for TiO_2 membrane in dark of 49.6 ng droplet.

Table 3.1 is a summary of the percent degradation of dye intensity over time for the four experimental conditions in triplicate. The standard deviations that were calculated in Table 3.1 were quite high, meaning the range of the data differed significantly from the calculated mean. However, the individual environments of each triplicate were identical, and the analysis method consistently yielded high quality calibration curves. A likely explanation for this is that the droplets were not uniformly drop-cast onto the membrane and caused an uneven distribution. What resulted was some areas of the droplet reached the upper limit of the linear region according to Beer's law. Over time, the areas with less dye would seemingly lose intensity more quickly than the areas with more dye, thereby yielding a smaller overall decrease in dye intensity.

Table 3.3: Percent degradation in mass for 30.9 ng and 42.2 ng droplets.

TiO_2 Dark			
36.3 ng droplet		49.6 ng droplet	
Exp	%deg	Exp	%deg
1	60.57	1	51.74
2	32.01	2	31.55
3	53.06	3	25.67
Ave	**48.55**	**Ave**	**36.32**
Std Dev	**14.81**	**Std Dev**	**13.67**

Ag/TiO_2 Dark			
36.3 ng droplet		49.6 ng droplet	
Exp	%deg	Exp	%deg
1	52.41	1	48.01
2	41.29	2	33.22
3	76.70	3	61.36
Ave	**56.80**	**Ave**	**47.53**
Std Dev	**18.11**	**Std Dev**	**14.08**

TiO_2 Light			
36.3 ng droplet		49.6 ng droplet	
Exp	%deg	Exp	%deg
1	43.59	1	27.39
2	40.00	2	49.96
3	40.90	3	36.73
Ave	**41.50**	**Ave**	**38.03**
Std Dev	**1.87**	**Std Dev**	**11.34**

Ag/TiO_2 Light			
36.3 ng droplet		49.6 ng droplet	
Exp	%deg	Exp	%deg
1	53.80	1	58.57
2	57.96	2	49.97
3	51.30	3	40.60
Ave	**54.35**	**Ave**	**49.71**
Std Dev	**3.36**	**Std Dev**	**8.99**

A higher percent decrease in mass was consistently observed in the 36.3 ng droplet than in the 49.6 ng droplet. This demonstrates that each methylene blue molecule that was broken down in the 36.3 ng droplet had more of an impact of the percent degradation, than in the larger sample. Ag/TiO_2 membranes were approximately 10% more effective in breaking down methylene blue in

dark and light environments for both dye droplets. This demonstrates that adding Ag_2O had a measurable impact of the efficacy of the TiO_2 membrane. When white light was added, there seemed to have no effect on the percent mass decrease of the dye. While this behavior was expected for TiO_2 membrane, it was not for the Ag/TiO_2 membrane. As aforementioned, incorporating Ag shortens the band gap, thereby red shifting the photocatalysts light activity range.[54] The band gap for the Ag/TiO_2 material was found to be 3.38 eV. As mentioned in the power densities of 320 nm and 365 nm of the white light were 0 mW/cm^2 for all four experimental conditions. So, while it was expected degradation percentages to be higher for Ag/TiO_2 light experiments and Ag/TiO_2 dark experiments, the results were equivalent to each other. Though the results falsified the hypothesis, they confirmed that the digital quantification acquired from the Gel Imaging System was reliable.

3.3.2.2 Droplet Size Change on Photocatalytic Surface under Different Conditions

The purpose of this analysis was to collect data that would point to a correlation between the percent mass decrease (Table 3.3) and the change in droplet size (Table 3.4). In the preliminary UV experiments, droplets sizes commonly increased over two-hour periods of time. While dye spreading will not affect the accuracy of the mass calculation as it did in preliminary UV studies, it deserves examination under a shorter timeframe. The standardized image-capturing allowed for droplet size to be tracked using area. For this experiment, the change in droplet size was calculated using Equation 8, where $Area_i$ is the initial area of the droplet and $Area_f$ is the final area. Due to the lower concentration of the droplets, the droplets were not perfectly rounded with smooth edges. This is why the area of the droplet was used instead of the diameter of the droplet.

$$\%Size\ Decrease = \frac{Area_i - Area_f}{Area_i} \times 100 \qquad Eq. 10$$

The averages across every experiment were positive. In most experimental environments, one triplicate of 36.3 ng and 49.6 ng droplets increased in size. The standard deviations were quite high, indicating the individual measurements varied greatly from mean and in most cases, they exceeded the average. In many cases, the size change did not directly relate to the decrease in mass on an individual or average basis. Because of this, it was determined that the droplet size change over time did not correlate to the percent mass decrease and is therefore not an appropriate analysis for this study.

Table 3.4: Percent Size decrease over 5 min for two droplets in Gel Imaging System study.

TiO_2 Dark			
36.3 ng droplet		49.6 ng droplet	
Exp	%Size Dec	Exp	%Size Dec
1	7.75	1	35.86
2	11.49	2	12.08
3	29.74	3	-13.19
Average	**16.33**	**Average**	**23.97**
Std Dev	**11.77**	**Std Dev**	**16.81**

Ag/TiO_2 Dark			
36.3 ng droplet		49.6 ng droplet	
Exp	%Size Dec	Exp	%Size Dec
1	4.49	1	20.46
2	34.22	2	7.21
3	20.21	3	2.78
Average	**19.36**	**Average**	**10.15**
Std Dev	**21.02**	**Std Dev**	**9.20**

TiO_2 Light			
36.3 ng droplet		49.6 ng droplet	
Exp	%Size Dec	Exp	%Size Dec
1	9.06	1	-6.70
2	8.91	2	42.34
3	-2.70	3	13.18
Average	**5.09**	**Average**	**17.82**
Std Dev	**6.75**	**Std Dev**	**34.68**

Ag/TiO_2 Light			
36.3 ng droplet		49.6 ng droplet	
Exp	%Size Dec	Exp	%Size Dec
1	-0.59	1	-4.41
2	-0.98	2	12.63
3	28.23	3	8.79
Average	**8.89**	**Average**	**4.11**
Std Dev	**16.75**	**Std Dev**	**12.05**

3.3.2.3 Kinetics of Dye on the Membranes under Different Conditions

Identifying the kinetics of methylene blue's fading over time was done by plotting 0^{th} order, 1^{st} order, and 2^{nd} order graphs and comparing the R^2 values of the linear regressions from those graphs for all Gel Imaging data sets. Derivations for these kinetics and rate constants can be found in the Appendix. Figures 3.20-3.22 show the typical kinetic analysis followed for all data sets. The

first order graphs were plotted to have an intercept set to 0. By doing this, R^2 values improved for all data sets. All data sets in all experimental environments yielded L-H 1st order results.

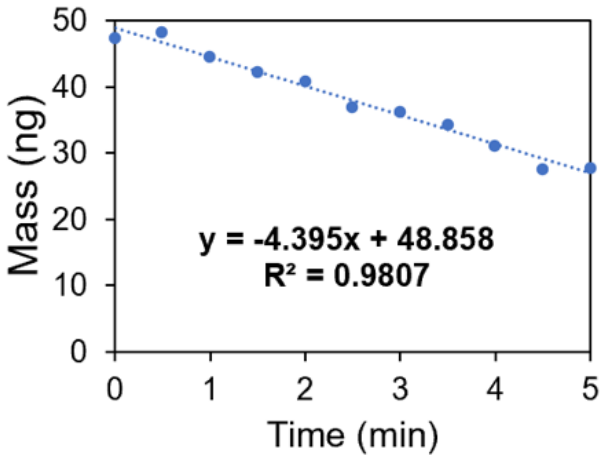

Figure 3.20: 0th order kinetic analysis of TiO_2 dark experiment 49.6 ng droplet.

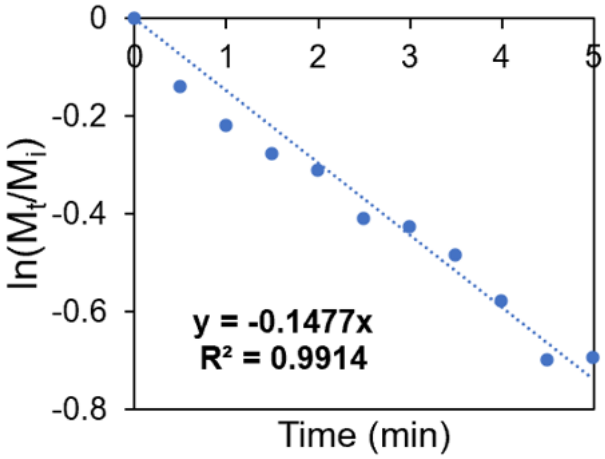

Figure 3.21: 1st order kinetic analysis of TiO_2 dark experiment 49.6 ng droplet where M_t is the mass at time t and M_i is the initial mass.

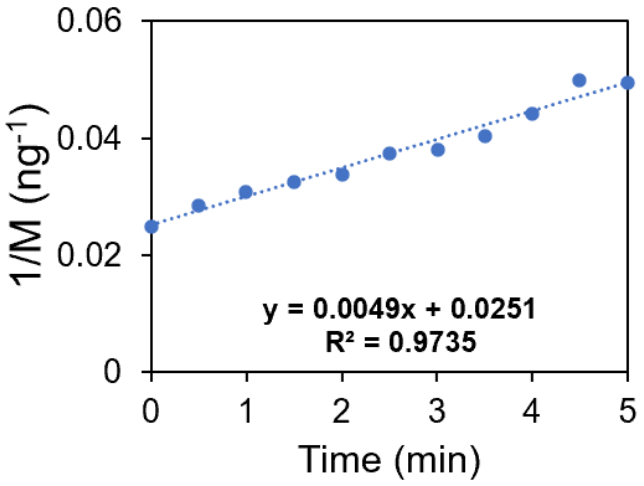

Figure 3.22: 2nd order kinetic analysis of TiO_2 dark experiment 42.2 ng droplet.

Table 3.5 is a collection of all kinetic information from all Gel Imaging experiments. All standard deviations were excellent. This indicated that though the droplet size and percent mass decrease were inconsistent, the digital quantification in the Gel Imaging System was still able to collect reproducible kinetic information for all experimental environments. In literature, rate constants for methylene blue in a TiO_2 suspension under UV range from 0.040 min^- to 0.0011 min^- .[42,60] All averaged rate constants were larger by at least one magnitude. This can be attributed to the excess photocatalyst, presence of water, and the basic nature of the membrane.

Because the dye was always in direct contact with the membrane, the experiments were considered to contain an excess amount of photocatalyst. The excess photocatalyst in the presence of excess water allowed for the constant generation of reactive oxygen species which were able to quickly breakdown methylene blue at the interface. A suspension requires stirring to allow the photocatalytic particles to reach the dye.

Table 3.5: All 1st order kinetic information for all Gel Imaging System experiments.

TiO_2 Dark				Ag/TiO_2 Dark			
36.3 ng droplet		49.6 ng droplet		36.3 ng droplet		49.6 ng droplet	
Exp	Slope	Exp	Slope	Exp	Slope	Exp	Slope
1	-0.1812	1	-0.1404	1	-0.1475	1	-0.1257
2	-0.0777	2	-0.0775	2	-0.2889	2	-0.1475
3	-0.1458	3	0.0588	3	-0.1163	3	-0.1933
Average	**-0.1349**	**Average**	**-0.1090**	**Average**	**-0.2182**	**Average**	**-0.1555**
k	**0.1349**	**k**	**0.1090**	**k**	**0.2182**	**k**	**0.1555**
Std Dev	**0.0526**	**Std Dev**	**0.0445**	**Std Dev**	**0.1000**	**Std Dev**	**0.0345**
TiO_2 Light				Ag/TiO_2 Light			
36.3 ng droplet		49.6 ng droplet		36.3 ng droplet		49.6 ng droplet	
Exp	Slope	Exp	Slope	Exp	Slope	Exp	Slope
1	-0.1058	1	-0.0598	1	-0.1785	1	-0.1920
2	-0.0937	2	-0.1681	2	-0.1654	2	-0.1477
3	-0.1083	3	-0.0756	3	-0.1430	3	0.1071
Average	**-0.1026**	**Average**	**-0.1140**	**Average**	**-0.1623**	**Average**	**-0.1699**
k	**0.1026**	**k**	**0.1140**	**k**	**0.1623**	**k**	**0.1699**
Std Dev	**0.0078**	**Std Dev**	**0.0766**	**Std Dev**	**0.0180**	**Std Dev**	**0.0313**

While previous studies, mentioned in the Appendix, revealed that water can quickly evaporate from the membrane no matter the light source, there was no evaporation with the Gel Imaging experiments. Figure 3.23 shows methylene blue on an Ag/TiO_2 membrane at 0 min and 5 min in a Light Experiment and is a visual depiction of the presence of water throughout the experiments. The light grey circles surrounding the droplets shows the presence of water and the true diameter of the 10 µL droplet. The white arrow labeled "0 ng MB" points to a 10 µL droplet of water that served as the background.[7,30,32,39,64,78,79]

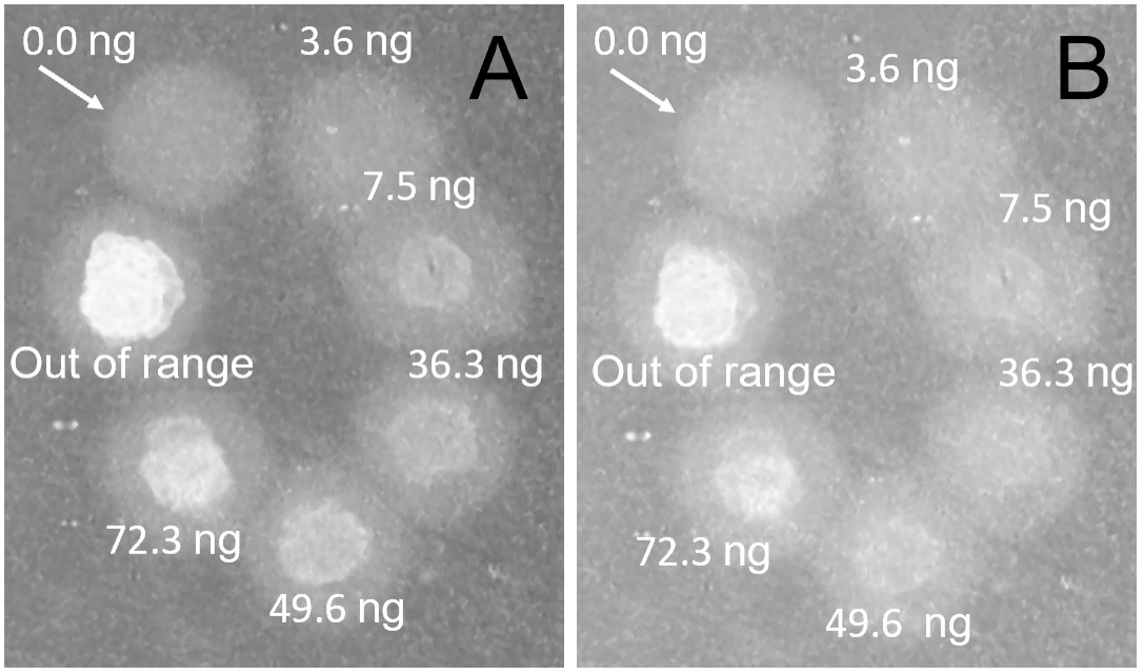

Figure 3.23: Methylene blue on Ag/TiO_2 membrane in a Light Experiment. The light grey circles indicate the presence of water.

4. Conclusion and Future Work

This study successfully developed a method to quantify the mass of methylene blue deposited on the solid membranes under different conditions. By utilizing ImageJ, calibration curves relating the mass of methylene blue to dye intensity were consistently collected. The calibration curves and the absorbances of the samples were used to calculate the mass of each dye droplet, whose averages were within ±3 ng of the samples' mass. The linear region of the calibration curve was found to be 0 – 72.3 ng of methylene blue. This method allowed further investigation of methylene blue on dry photocatalytic surfaces, that is, TiO_2 and Ag/TiO_2 self-assembled membranes. Due to the basic environment, the Ag in the membrane is oxidized and the amount is below detection limit. Therefore, we didn't observe substantial difference between the two membranes. The degradation of dye in dark follows first kinetics; however, we didn't observe photocatalytic activity under

visible irradiation possibly due to the low light intensity and inhomogeneity of the dye droplet mass. Future studies could include work towards optimization of the method for the increase of the homogeneity of the dye on the membranes, identification of the linear regions for other dyes such as methyl orange or rhodamine B, and the use of it to assess the membranes made of photocatalysts other than TiO_2.

References

(1) Lee, S. Y.; Park, S. J. TiO2 Photocatalyst for Water Treatment Applications. *Journal of Industrial and Engineering Chemistry*. November 25, 2013, pp 1761–1769. https://doi.org/10.1016/j.jiec.2013.07.012.

(2) Pelaez, M.; Nolan, N. T.; Pillai, S. C.; Seery, M. K.; Falaras, P.; Kontos, A. G.; Dunlop, P. S. M.; Hamilton, J. W. J.; Byrne, J. A.; O'Shea, K.; Entezari, M. H.; Dionysiou, D. D. A Review on the Visible Light Active Titanium Dioxide Photocatalysts for Environmental Applications. *Applied Catalysis B: Environmental*. August 21, 2012, pp 331–349. https://doi.org/10.1016/j.apcatb.2012.05.036.

(3) Han, F.; Kambala, V. S. R.; Srinivasan, M.; Rajarathnam, D.; Naidu, R. Tailored Titanium Dioxide Photocatalysts for the Degradation of Organic Dyes in Wastewater Treatment: A Review. *Applied Catalysis A: General*. May 15, 2009, pp 25–40. https://doi.org/10.1016/j.apcata.2009.02.043.

(4) Li, R.; Li, T.; Zhou, Q. Impact of Titanium Dioxide (TiO2) Modification on Its Application to Pollution Treatment—a Review. *Catalysts*. MDPI July 1, 2020. https://doi.org/10.3390/catal10070804.

(5) Ochiai, T.; Hoshi, T.; Slimen, H.; Nakata, K.; Murakami, T.; Tatejima, H.; Koide, Y.; Houas, A.; Horie, T.; Morito, Y.; Fujishima, A. Fabrication of a TiO2 Nanoparticles Impregnated Titanium Mesh Filter and Its Application for Environmental Purification. *Catal Sci Technol* **2011**, *1* (8), 1324–1327. https://doi.org/10.1039/c1cy00185j.

(6) Nyamutswa, L. T.; Hanson, B.; Navaratna, D.; Collins, S. F.; Linden, K. G.; Duke, M. C. Sunlight-Transmitting Photocatalytic Membrane for Reduced Maintenance Water

Treatment. *ACS ES and T Water* **2021**, *1* (9), 2001–2011. https://doi.org/10.1021/acsestwater.1c00073.

(7) Nyamutswa, L. T.; Zhu, B.; Collins, S. F.; Navaratna, D.; Duke, M. C. Light Conducting Photocatalytic Membrane for Chemical-Free Fouling Control in Water Treatment. *J Memb Sci* **2020**, *604*. https://doi.org/10.1016/j.memsci.2020.118018.

(8) *Waterborne Diseases: Facts & How to Help | World Vision Canada*. https://www.worldvision.ca/stories/clean-water/cholera-waterborne-disease-facts (accessed 2023-11-06).

(9) Schneider, J.; Matsuoka, M.; Takeuchi, M.; Zhang, J.; Horiuchi, Y.; Anpo, M.; Bahnemann, D. W. Understanding TiO2photocatalysis: Mechanisms and Materials. *Chemical Reviews*. American Chemical Society October 8, 2014, pp 9919–9986. https://doi.org/10.1021/cr5001892.

(10) Tong, H.; Ouyang, S.; Bi, Y.; Umezawa, N.; Oshikiri, M.; Ye, J. Nano-Photocatalytic Materials: Possibilities and Challenges. *Advanced Materials* **2012**, *24* (2), 229–251. https://doi.org/10.1002/adma.201102752.

(11) Hone, F. G.; Dejene, F. B. Cationic Concentration and PH Effect on the Structural, Morphological and Optical Band Gap of Chemically Synthesized Lead Sulfide Thin Films. *Journal of Materials Research and Technology* **2019**, *8* (1), 467–474. https://doi.org/10.1016/j.jmrt.2018.03.004.

(12) Nyamutswa, L. T.; Zhu, B.; Collins, S. F.; Navaratna, D.; Duke, M. C. Light Conducting Photocatalytic Membrane for Chemical-Free Fouling Control in Water Treatment. *J Memb Sci* **2020**, *604*. https://doi.org/10.1016/j.memsci.2020.118018.

(13) Navidpour, A. H.; Abbasi, S.; Li, D.; Mojiri, A.; Zhou, J. L. Investigation of Advanced Oxidation Process in the Presence of TiO2 Semiconductor as Photocatalyst: Property, Principle, Kinetic Analysis, and Photocatalytic Activity. *Catalysts*. MDPI February 1, 2023. https://doi.org/10.3390/catal13020232.

(14) Schneider, J.; Matsuoka, M.; Takeuchi, M.; Zhang, J.; Horiuchi, Y.; Anpo, M.; Bahnemann, D. W. Understanding TiO2photocatalysis: Mechanisms and Materials. *Chemical Reviews*. American Chemical Society October 8, 2014, pp 9919–9986. https://doi.org/10.1021/cr5001892.

(15) Linsebigler, A. L.; Lu, G.; Yates, J. T. *Photocatalysis on Ti02 Surfaces: Principles, Mechanisms, and Selected Results*; 1995; Vol. 95. https://pubs.acs.org/sharingguidelines.

(16) Tachikawa, T.; Yamashita, S.; Majima, T. Evidence for Crystal-Face-Dependent TiO2 Photocatalysis from Single-Molecule Imaging and Kinetic Analysis. *J Am Chem Soc* **2011**, *133* (18), 7197–7204. https://doi.org/10.1021/ja201415j.

(17) Opoku, F.; Govender, K. K.; van Sittert, C. G. C. E.; Govender, P. P. Recent Progress in the Development of Semiconductor-Based Photocatalyst Materials for Applications in Photocatalytic Water Splitting and Degradation of Pollutants. *Advanced Sustainable Systems*. Wiley-VCH Verlag July 1, 2017. https://doi.org/10.1002/adsu.201700006.

(18) Basavarajappa, P. S.; Patil, S. B.; Ganganagappa, N.; Reddy, K. R.; Raghu, A. V.; Reddy, C. V. Recent Progress in Metal-Doped TiO2, Non-Metal Doped/Codoped TiO2 and TiO2 Nanostructured Hybrids for Enhanced Photocatalysis. *Int J Hydrogen Energy* **2020**, *45* (13), 7764–7778. https://doi.org/10.1016/j.ijhydene.2019.07.241.

(19) Makuła, P.; Pacia, M.; Macyk, W. How To Correctly Determine the Band Gap Energy of Modified Semiconductor Photocatalysts Based on UV-Vis Spectra. *Journal of Physical Chemistry Letters*. American Chemical Society December 6, 2018, pp 6814–6817. https://doi.org/10.1021/acs.jpclett.8b02892.

(20) Makuła, P.; Pacia, M.; Macyk, W. How To Correctly Determine the Band Gap Energy of Modified Semiconductor Photocatalysts Based on UV-Vis Spectra. *Journal of Physical Chemistry Letters*. American Chemical Society December 6, 2018, pp 6814–6817. https://doi.org/10.1021/acs.jpclett.8b02892.

(21) Tian, Z. R.; Voigt, J. A.; Liu, J.; McKenzie, B.; Xu, H. Large Oriented Arrays and Continuous Films of TiO2-Based Nanotubes. *J Am Chem Soc* **2003**, *125* (41), 12384–12385. https://doi.org/10.1021/ja0369461.

(22) Ng, J.; Wang, X.; Sun, D. D. One-Pot Hydrothermal Synthesis of a Hierarchical Nanofungus-like Anatase TiO2 Thin Film for Photocatalytic Oxidation of Bisphenol A. *Appl Catal B* **2011**, *110*, 260–272. https://doi.org/10.1016/j.apcatb.2011.09.011.

(23) Zhao, Z.; Li, Z.; Zou, Z. Structure and Properties of Water on the Anatase TiO 2(101) Surface: From Single-Molecule Adsorption to Interface Formation. *Journal of Physical Chemistry C* **2012**, *116* (20), 11054–11061. https://doi.org/10.1021/jp301468c.

(24) Linsebigler, A. L.; Lu, G.; Yates, J. T. *Photocatalysis on Ti02 Surfaces: Principles, Mechanisms, and Selected Results*; 1995; Vol. 95. https://pubs.acs.org/sharingguidelines.

(25) Nyamutswa, L. T.; Hanson, B.; Navaratna, D.; Collins, S. F.; Linden, K. G.; Duke, M. C. Sunlight-Transmitting Photocatalytic Membrane for Reduced Maintenance Water

Treatment. *ACS ES and T Water* **2021**, *1* (9), 2001–2011. https://doi.org/10.1021/acsestwater.1c00073.

(26) Ochiai, T.; Hoshi, T.; Slimen, H.; Nakata, K.; Murakami, T.; Tatejima, H.; Koide, Y.; Houas, A.; Horie, T.; Morito, Y.; Fujishima, A. Fabrication of a TiO2 Nanoparticles Impregnated Titanium Mesh Filter and Its Application for Environmental Purification. *Catal Sci Technol* **2011**, *1* (8), 1324–1327. https://doi.org/10.1039/c1cy00185j.

(27) Lee, S. Y.; Park, S. J. TiO2 Photocatalyst for Water Treatment Applications. *Journal of Industrial and Engineering Chemistry*. November 25, 2013, pp 1761–1769. https://doi.org/10.1016/j.jiec.2013.07.012.

(28) Li, Z.; Cong, S.; Xu, Y. Brookite vs Anatase TiO2 in the Photocatalytic Activity for Organic Degradation in Water. *ACS Catal* **2014**, *4* (9), 3273–3280. https://doi.org/10.1021/cs500785z.

(29) Khanna, A.; Shetty, V. K. Solar Light Induced Photocatalytic Degradation of Reactive Blue 220 (RB-220) Dye with Highly Efficient Ag@TiO2 Core-Shell Nanoparticles: A Comparison with UV Photocatalysis. *Solar Energy* **2014**, *99*, 67–76. https://doi.org/10.1016/j.solener.2013.10.032.

(30) Qin, X.; Jing, L.; Tian, G.; Qu, Y.; Feng, Y. Enhanced Photocatalytic Activity for Degrading Rhodamine B Solution of Commercial Degussa P25 TiO2 and Its Mechanisms. *J Hazard Mater* **2009**, *172* (2–3), 1168–1174. https://doi.org/10.1016/j.jhazmat.2009.07.120.

(31) Natarajan, T. S.; Thomas, M.; Natarajan, K.; Bajaj, H. C.; Tayade, R. J. Study on UV-LED/TiO2 Process for Degradation of Rhodamine B Dye. *Chemical Engineering Journal* **2011**, *169* (1–3), 126–134. https://doi.org/10.1016/j.cej.2011.02.066.

(32) Mohabansi, N. P.; Patil, V. B.; Yenkie, N. A COMPARATIVE STUDY ON PHOTO DEGRADATION OF METHYLENE BLUE DYE EFFLUENT BY ADVANCED OXIDATION PROCESS BY USING TiO 2 /ZnO PHOTO CATALYST. **2011**, *4* (4), 814–819.

(33) Kinetic and Mechanistic Study of TiO2.

(34) Mohabansi, N. P.; Patil, V. B.; Yenkie, N. A COMPARATIVE STUDY ON PHOTO DEGRADATION OF METHYLENE BLUE DYE EFFLUENT BY ADVANCED OXIDATION PROCESS BY USING TiO 2 /ZnO PHOTO CATALYST. **2011**, *4* (4), 814–819.

(35) Rajagopal, S.; Paramasivam, B.; Muniyasamy, K. Photocatalytic Removal of Cationic and Anionic Dyes in the Textile Wastewater by H2O2 Assisted TiO2 and Micro-Cellulose Composites. *Sep Purif Technol* **2020**, *252*. https://doi.org/10.1016/j.seppur.2020.117444.

(36) Owa, F. D. Water Pollution: Sources, Effects, Control and Management. *Mediterr J Soc Sci* **2013**, *4* (8), 65–68. https://doi.org/10.5901/mjss.2013.v4n8p65.

(37) Gümüş, D.; Akbal, F. Photocatalytic Degradation of Textile Dye and Wastewater. *Water Air Soil Pollut* **2011**, *216* (1–4), 117–124. https://doi.org/10.1007/s11270-010-0520-z.

(38) Fernández, C.; Larrechi, M. S.; Callao, M. P. An Analytical Overview of Processes for Removing Organic Dyes from Wastewater Effluents. *TrAC - Trends in Analytical Chemistry*. November 2010, pp 1202–1211. https://doi.org/10.1016/j.trac.2010.07.011.

(39) Wu, C. H.; Chern, J. M. Kinetics of Photocatalytic Decomposition of Methylene Blue. *Ind Eng Chem Res* **2006**, *45* (19), 6450–6457. https://doi.org/10.1021/ie0602759.

(40) Nogueira, R. F. P.; Jardim, W. F. Photodegradation of Methylene Blue: Using Solar Light and Semiconductor (TiO2). *J Chem Educ* **1993**, *70* (10), 863–864. https://doi.org/10.1021/ed070p861.

(41) Eddy, D. R.; Permana, M. D.; Sakti, L. K.; Sheha, G. A. N.; Solihudin, G. A. N.; Hidayat, S.; Takei, T.; Kumada, N.; Rahayu, I. Heterophase Polymorph of TiO2 (Anatase, Rutile, Brookite, TiO2 (B)) for Efficient Photocatalyst: Fabrication and Activity. *Nanomaterials*. MDPI February 1, 2023. https://doi.org/10.3390/nano13040704.

(42) Lakshmi Renganathan, S. R. Study on TiO2-Mediated Photocatalytic Degradation of Methylene Blue. *Journal of Photochemistry and Photobiology ~cnmmm, ax ELSEVIER A: Chemistry* **1995**, *88*, 163–167.

(43) Siah, W. R.; Lintang, H. O.; Shamsuddin, M.; Yuliati, L. High Photocatalytic Activity of Mixed Anatase-Rutile Phases on Commercial TiO2 Nanoparticles. In *IOP Conference Series: Materials Science and Engineering*; Institute of Physics Publishing, 2016; Vol. 107. https://doi.org/10.1088/1757-899X/107/1/012005.

(44) Pelaez, M.; Nolan, N. T.; Pillai, S. C.; Seery, M. K.; Falaras, P.; Kontos, A. G.; Dunlop, P. S. M.; Hamilton, J. W. J.; Byrne, J. A.; O'Shea, K.; Entezari, M. H.; Dionysiou, D. D. A Review on the Visible Light Active Titanium Dioxide Photocatalysts for Environmental Applications. *Applied Catalysis B: Environmental*. August 21, 2012, pp 331–349. https://doi.org/10.1016/j.apcatb.2012.05.036.

(45) Nosheen, S.; Galasso, F. S.; Suib, S. L. Role of Ti-O Bonds in Phase Transitions of TiO 2. *Langmuir* **2009**, *25* (13), 7623–7630. https://doi.org/10.1021/la9002719.

(46) Dambournet, D.; Belharouak, I.; Amine, K. Tailored Preparation Methods of TiO2 Anatase, Rutile, Brookite: Mechanism of Formation and Electrochemical Properties. *Chemistry of Materials* **2010**, *22* (3), 1173–1179. https://doi.org/10.1021/cm902613h.

(47) Shahrezaei, M.; Habibzadeh, S.; Babaluo, A. A.; Hosseinkhani, H.; Haghighi, M.; Hasanzadeh, A.; Tahmasebpour, R. Study of Synthesis Parameters and Photocatalytic Activity of TiO2 Nanostructures. *J Exp Nanosci* **2017**, *12* (1), 45–61. https://doi.org/10.1080/17458080.2016.1258495.

(48) Ghosh, A.; Mohammed, O. F.; Bakr, O. M. Atomic-Level Doping of Metal Clusters. *Acc Chem Res* **2018**, *51* (12), 3094–3103. https://doi.org/10.1021/acs.accounts.8b00412.

(49) Nosaka, Y.; Nosaka, A. Y. Reconsideration of Intrinsic Band Alignments within Anatase and Rutile TiO2. *Journal of Physical Chemistry Letters*. American Chemical Society February 4, 2016, pp 431–434. https://doi.org/10.1021/acs.jpclett.5b02804.

(50) Barone, P.; Stranges, F.; Barberio, M.; Renzelli, D.; Bonanno, A.; Xu, F. Study of Band Gap of Silver Nanoparticles - Titanium Dioxide Nanocomposites. *J Chem* **2014**, *2014*. https://doi.org/10.1155/2014/589707.

(51) Lin, T. H.; Wu, M. C.; Chiang, K. P.; Chang, Y. H.; Hsu, J. F.; Hsu, K. H.; Lee, K. M. Unveiling the Surface Precipitation Effect of Ag Ions in Ag-Doped TiO2 Nanofibers Synthesized by One-Step Hydrothermal Method for Photocatalytic Hydrogen Production. *J Taiwan Inst Chem Eng* **2021**, *120*, 291–299. https://doi.org/10.1016/j.jtice.2021.03.011.

(52) Yang, X. J.; Wang, S.; Sun, H. M.; Wang, X. B.; Lian, J. S. Preparation and Photocatalytic Performance of Cu-Doped TiO2 Nanoparticles. *Transactions of Nonferrous Metals Society*

of China (English Edition) **2015**, *25* (2), 504–509. https://doi.org/10.1016/S1003-6326(15)63631-7.

(53) Yang, X. J.; Wang, S.; Sun, H. M.; Wang, X. B.; Lian, J. S. Preparation and Photocatalytic Performance of Cu-Doped TiO2 Nanoparticles. *Transactions of Nonferrous Metals Society of China (English Edition)* **2015**, *25* (2), 504–509. https://doi.org/10.1016/S1003-6326(15)63631-7.

(54) Tryba, B.; Piszcz, M.; Morawski, A. W. Photocatalytic and Self-Cleaning Properties of Ag-Doped Tio2. *Open Materials Science Journal* **2010**, *4*, 5–8. https://doi.org/10.2174/1874088X01004020005.

(55) Zakir, O.; Ait Karra, A.; Idouhli, R.; Elyaagoubi, M.; Khadiri, M.; Dikici, B.; Aityoub, A.; Abouelfida, A.; Outzourhit, A. Fabrication and Characterization of Ag- and Cu-Doped TiO2 Nanotubes (NTs) by in Situ Anodization Method as an Efficient Photocatalyst. *Journal of Solid State Electrochemistry* **2022**, *26* (10), 2247–2260. https://doi.org/10.1007/s10008-022-05237-4.

(56) Chen, F.; Schafranek, R.; Wu, W.; Klein, A. Reduction-Induced Fermi Level Pinning at the Interfaces between Pb(Zr,Ti)O3 and Pt, Cu and Ag Metal Electrodes. *J Phys D Appl Phys* **2011**, *44* (25). https://doi.org/10.1088/0022-3727/44/25/255301.

(57) Kahn, A. Fermi Level, Work Function and Vacuum Level. *Materials Horizons*. Royal Society of Chemistry January 1, 2016, pp 7–10. https://doi.org/10.1039/c5mh00160a.

(58) Heger, D.; Jirkovský, J.; Klán, P. Aggregation of Methylene Blue in Frozen Aqueous Solutions Studied by Absorption Spectroscopy. *Journal of Physical Chemistry A* **2005**, *109* (30), 6702–6709. https://doi.org/10.1021/jp050439j.

(59) Le, S. T. T.; Khanitchaidecha, W.; Nakaruk, A. Photocatalytic Reactor for Organic Compound Removal Using Photocatalytic Mechanism. *Bulletin of Materials Science* **2016**, *39* (2), 569–572. https://doi.org/10.1007/s12034-016-1158-2.

(60) Chang, H.; Su, C.; Lo, C.-H.; Chen, L.-C.; Tsung, T.-T.; Jwo, C.-S. *Photodecomposition and Surface Adsorption of Methylene Blue on TiO 2 Nanofluid Prepared by ASNSS*.

(61) Svitková, V.; Vyskočil, V. Electrochemical Behavior of Methylene Blue at Bare and DNA-Modified Silver Solid Amalgam Electrodes. *Journal of Solid State Electrochemistry* **2022**, *26* (11), 2491–2499. https://doi.org/10.1007/s10008-022-05270-3.

(62) Mahlum, J. D.; Pellitero, M. A.; Arroyo-Currás, N. Chemical Equilibrium-Based Mechanism for the Electrochemical Reduction of DNA-Bound Methylene Blue Explains Double Redox Waves in Voltammetry. *Journal of Physical Chemistry C* **2021**, *125* (17), 9038–9049. https://doi.org/10.1021/acs.jpcc.1c00336.

(63) Li Puma, G.; Yue, P. L. Modelling and Design of Thin-Film Slurry Photocatalytic Reactors for Water Purification. *Chem Eng Sci* **2003**, *58* (11), 2269–2281. https://doi.org/10.1016/S0009-2509(03)00086-1.

(64) Mozia, S.; Toyoda, M.; Inagaki, M.; Tryba, B.; Morawski, A. W. Application of Carbon-Coated TiO2 for Decomposition of Methylene Blue in a Photocatalytic Membrane Reactor. *J Hazard Mater* **2007**, *140* (1–2), 369–375. https://doi.org/10.1016/j.jhazmat.2006.10.016.

(65) *Analyze Menu*. https://imagej.nih.gov/ij/docs/menus/analyze.html (accessed 2023-09-27).

(66) Li, M.; Noriega-Trevino, M. E.; Nino-Martinez, N.; Marambio-Jones, C.; Wang, J.; Damoiseaux, R.; Ruiz, F.; Hoek, E. M. V. Synergistic Bactericidal Activity of Ag-TiO 2

Nanoparticles in Both Light and Dark Conditions. *Environ Sci Technol* **2011**, *45* (20), 8989–8995. https://doi.org/10.1021/es201675m.

(67) Liu, C. H.; Hong, M. H.; Zhou, Y.; Chen, G. X.; Saw, M. M.; Hor, A. T. S. Synthesis and Characterization of Ag Deposited TiO2 Particles by Laser Ablation in Water. In *Physica Scripta T*; 2007; Vol. T129, pp 326–328. https://doi.org/10.1088/0031-8949/2007/T129/072.

(68) You, X.; Chen, F.; Zhang, J.; Anpo, M. A Novel Deposition Precipitation Method for Preparation of Ag-Loaded Titanium Dioxide. *Catal Letters* **2005**, *102* (3–4), 247–250. https://doi.org/10.1007/s10562-005-5863-5.

(69) Thamaphat, K.; Limsuwan, P.; Ngotawornchai, B. *Phase Characterization of TiO 2 Powder by XRD and TEM*; 2008; Vol. 42.

(70) Behnajady, M. A.; Modirshahla, N.; Shokri, M. *ENHANCEMENT OF PHOTOCATALYTIC ACTIVITY OF TiO 2 NANOPARTICLES BY SILVER DOPING: PHOTODEPOSITION VERSUS LIQUID IMPREGNATION METHODS*; 2008; Vol. 10.

(71) Tobaldi, D. M.; Pullar, R. C.; Seabra, M. P.; Labrincha, J. A. Fully Quantitative X-Ray Characterisation of Evonik Aeroxide TiO 2 P25®. *Mater Lett* **2014**, *122*, 345–347. https://doi.org/10.1016/j.matlet.2014.02.055.

(72) Gauri, B.; Vidya, K.; Sharada, D.; Shobha, W. *October (2016) Res*; 2016; Vol. 20. https://www.researchgate.net/publication/319502481.

(73) Matsui, M.; Akaogi, M. Molecular Dynamics Simulation of the Structural and Physical Properties of the Four Polymorphs of Tio2. *Mol Simul* **1991**, *6* (4–6), 239–244. https://doi.org/10.1080/08927029108022432.

(74) Selçuk, S.; Selloni, A. Excess Electrons at Anatase TiO2 Surfaces and Interfaces: Insights from First Principles Simulations. *Journal of Physics D: Applied Physics*. Institute of Physics Publishing June 21, 2017. https://doi.org/10.1088/1361-6463/aa7540.

(75) *Supporting Information Ag Ag R = Rutile Ag = Silver*.

(76) Zubrick, J. W. *THE ORGANIC CHEM LAB SURVIVAL MANUAL A Student's Guide to Techniques*.

(77) AIST. *Spectral Database for Organic Compounds SDBS*.

(78) Chin, S.; Park, E.; Kim, M.; Jurng, J. Photocatalytic Degradation of Methylene Blue with TiO2 Nanoparticles Prepared by a Thermal Decomposition Process. *Powder Technol* **2010**, *201* (2), 171–176. https://doi.org/10.1016/j.powtec.2010.03.034.

(79) Zhao, D.; Yang, X.; Chen, C.; Wang, X. Enhanced Photocatalytic Degradation of Methylene Blue on Multiwalled Carbon Nanotubes-TiO2. *J Colloid Interface Sci* **2013**, *398*, 234–239. https://doi.org/10.1016/j.jcis.2013.02.017.

Appendices

Appendix A: Additional Experiments

A1. Methods

The following amounts of methylene blue were drop-cast on a TiO_2 membrane: 200 μg, 500 μg, 1000 μg, 1500 μg, and 2000 μg in 10 μL aqueous solution. The membrane was placed in a dark drawer for 2 h and used as a control. For another membrane, 10 μL of 2000 μg of methylene blue was drop-cast on and subjected to irradiation under a UV lamp for 2 h. Every 30 min, an additional 2000 μg of methylene blue in 10 μL aqueous solution was placed on the membrane. Images were taken using portrait, natural light settings in iPhone and then analyzed in ImageJ.

A TiO_2 membrane, 10 μL of 2000 μg of methylene blue was drop-cast on and subjected to irradiation under a UV lamp for 2 h. Every 30 min, an additional 2000 μg of methylene blue in 10 μL aqueous solution was placed on the membrane. Images were taken using portrait, natural light settings in iPhone and then analyzed in ImageJ. The droplets' GVs were used in this experiment because it was impossible to collect an accurate area of each droplet. This would have led to incorrect intensity measurements.

A2. Digital Qualification of Calibration Curve by iPhone and ImageJ

The purpose of these experiments was identify a relationship between color intensity and concentration using an iPhone and ImageJ. Figure A1 shows the images taken from this experiment. Figure A2 is the calibration curve of the grey values associated with the concentration of dye. Unfortunately, the regression line was not linear. Plateauing began at 50 ppm and continued more drastically with the increase in concentration. The white and yellow light surrounding the membrane is a reflection of the light source in the petri dish that contained the membrane. I tis possible the light reflection caused inconsistencies in the ImageJ analysis.

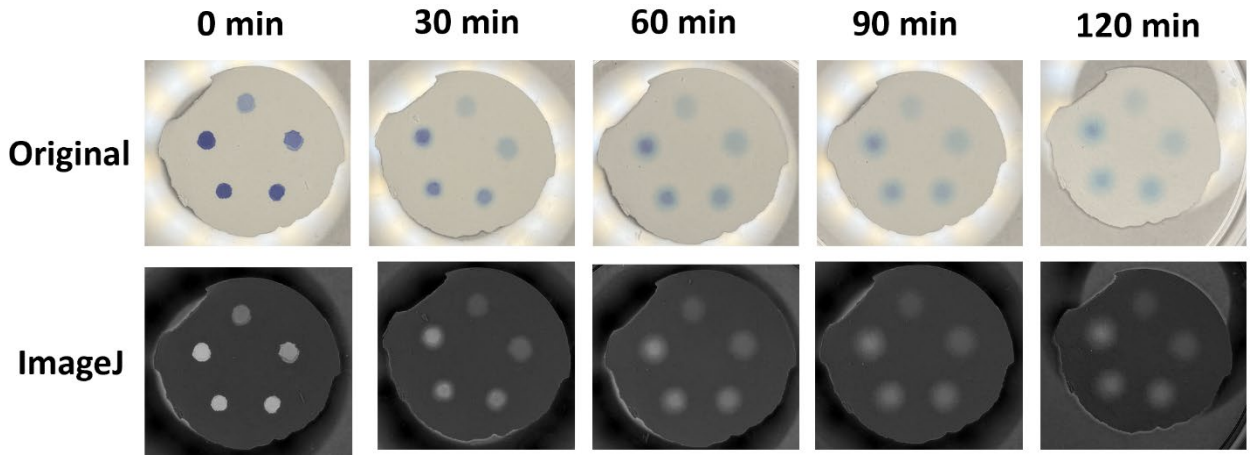

Figure A1: Calibration curve found at 0 min for methylene blue quantities at 200 µg, 500 µg, 1000 µg, 1500 µg, and 2000 µg in 10 µL aliquots. Images at 30 min, 60 min, 90 min and 120 min show the dyes fading while in the dark. The top row shows the images taken directly with iPhone. The bottom row shows images in grey scale and inverted in ImageJ.

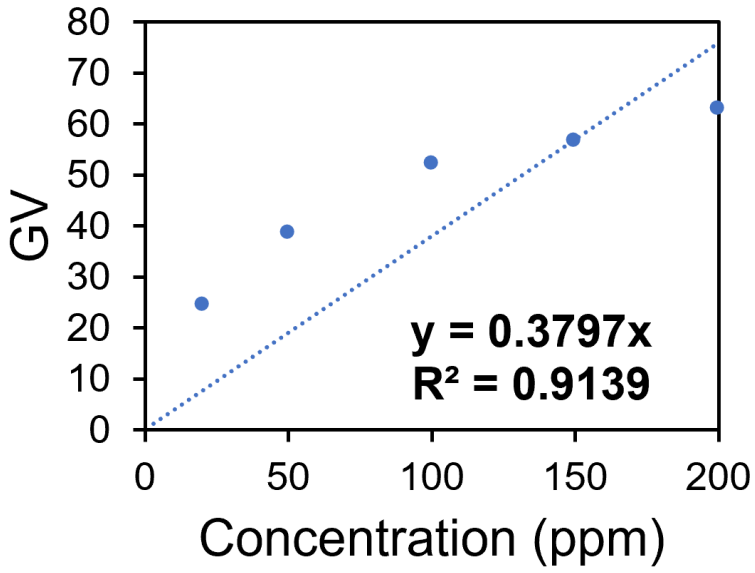

Figure A2: Calibration curve for low-powdered. The concentrations correspond directly to the droplets found in Figure A1. The intercept for the linear regression was set to 0.

Correcting each droplet's GV involved collecting an averaged GV for the membrane without dye that served as the background. Each background GV yielded standard deviations that did not fall within one to two standard deviations from the mean. We believe this gravely affected the results. Though in the dark, the dye faded over time. This is evidence for the formation of *leuco*-methylene blue. Another possibility for the observed plateau is that the dye is too concentrated and is therefore not within the linear region.

In the preliminary digital quantification studies, the dye droplets' size changed over time. Dye spreading was very apparent in the UV experiments as seen in Figure B3. This figure shows two images from a 2 h UV experiment at 0 min and 120 min studying a 10 µL droplet containing 500 µg of methylene blue. The diameter of the droplets and membranes were measured at their widest using ImageJ.

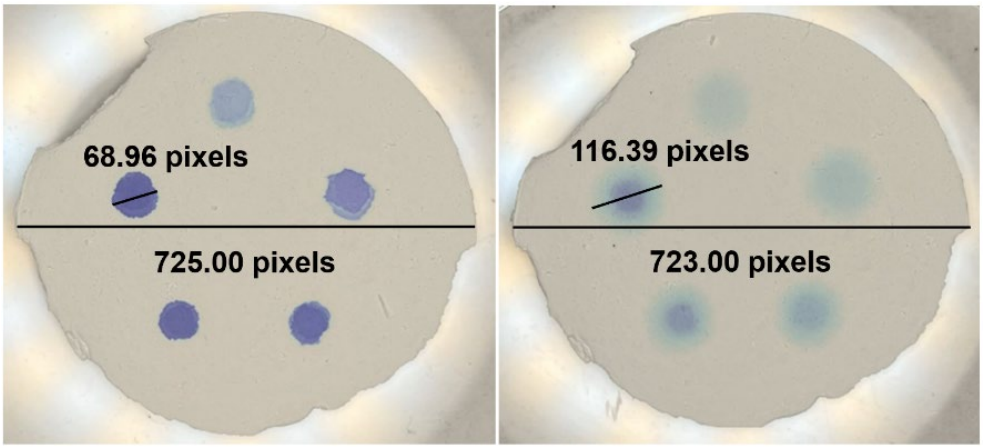

Figure A3: Images from 2 h UV experiment. The diameters of the droplet and membrane were measured using ImageJ. The droplet measurement ranged from 68.96 pixels to 116.39 pixels in width.

Because this image capturing was not standardized, the iPhone lens was not at the same distance from the membrane. This varied distance directly affects the pixel count and therefore,

utilizing the droplet's area would yield inaccurate data. To counteract this systematic error, we decided to examine the diameter of the droplet to diameter of the membrane percentage. At 0 min, the droplet's diameter was found to be 9.51% of the membrane's diameter; over time, that percentage increased to 16.10%. Though we observed a diameter increase, we still see the dye fading. We expected to observe a decrease in the diameter of the dye droplets. This is yet another reason to examine the intensity of the mass of dye, instead of the intensity of the concentration.

A3. Internal Standard experiment for UV light

Because calibration curve was not collected in earlier experiments, a percent GV reduction over time was calculated under the low power density (0.0174 W/cm^2), UV lamp. The experiment was composed of triplicates, utilizing an internal standard to accomplish this goal. The hypothesis was that there would be a high percent reduction of the dye's GV over 2 h. Figure A4 shows the photographic results from the low-powered, UV light experiment.

The first observation to be made is that after 30 m the dye does not seem to degrade as drastically. In fact, it seems that the dye faded more thoroughly in the dark than under UV. Figure A3 shows the percent decrease in GV over time, and it confirms the first observation. At 30 minutes and 120 m, the difference between the GVs of the sample and internal standard was 36.8% and 48.9%, respectively. The second observation to be made is the edges of the droplets seemed to be more defined than in Figure A3.

One possibility is that the UV lamp caused a slight increase in temperature in the membrane and caused the water to evaporate from the dye. By removing this crucial reactant, we removed a source for ROSs and the reaction slowed dramatically. Quantitative data was not collected in this experiment; however, the qualitative information provided reasonable conclusions from this set of

experiments. This experiment indicated that an internal standard has the potential to reveal quantitative information if it is accompanied by calibration curve.

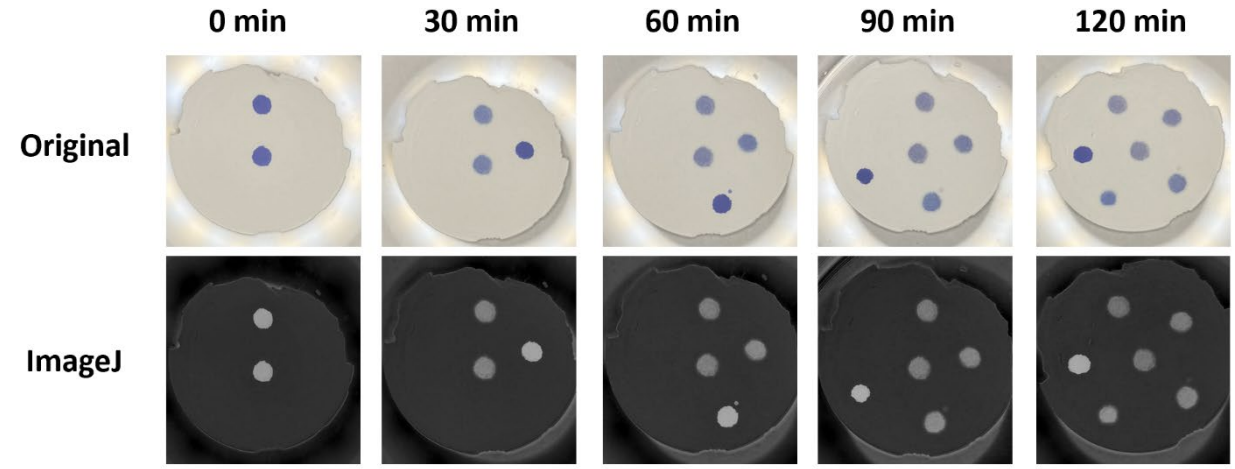

Figure A4: Images of internal standard experiment where experimental droplet is in the center of the membrane while the internal standard was placed before every image was taken.

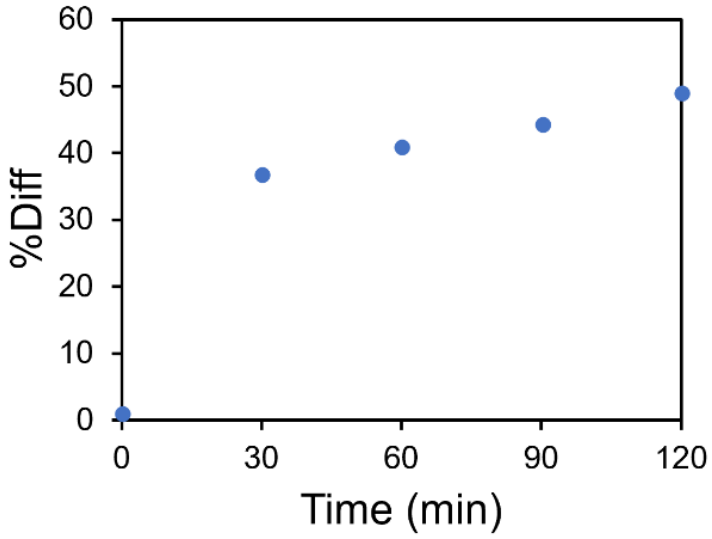

Figure A5: Percent difference between the sample and internal standard over time.

A4. Artificial Sunlight experiment

A TiO_2 membrane was hung vertically after 100 μL of 500 μg of methylene blue was drop-cast on it. The membrane was then exposed to a high-powered (300 W) Xe lamp to mimic sunlight for 90 min. The light spectrum of this light source can be found in the Appendix B. The power density was not acquired because the power meter required a specific wavelength to measure. The membrane was sprayed with water every 15 m while images were taken every 30 m. Images were taken using portrait, natural light settings in iPhone and then analyzed in ImageJ. The droplets' GVs were used in this experiment because it was impossible to collect an accurate area of each droplet. This would have led to incorrect intensity measurements.

This experiment tested the efficacy of a wet TiO_2 membrane in artificial light over time. The hypothesis was that the 100 μL of 50 ppm of methylene blue would degrade more quickly on a wet membrane due to the excess source for hydroxyl radicals, and that by taking the image of the membrane on a black sheet of paper, the extraneous reflected light would be eliminated. While the band gap for the membrane was quite low as compared to literature, the assumption was that the artificial sunlight would increase the overall efficiency of the membrane due to the light spectrum of the Xenon lamp.

Figure A6 shows the membrane at 0 m and at 60 m with an obvious change in color intensity. Figure A7 is a graph that shows the percent difference of GV over time. Within the first 15 m, the percentage difference in grey value was 55.5%. By the end of the experiment, the change was 68.0%. Though different light sources were used, Figures A5 and A7 have very similar patterns with plateauing after 30 and 15 m, respectively. Most likely, a majority of the TiO_2-methylene blue breakdown occurs within the first 15 m of light exposure no matter what the light source.

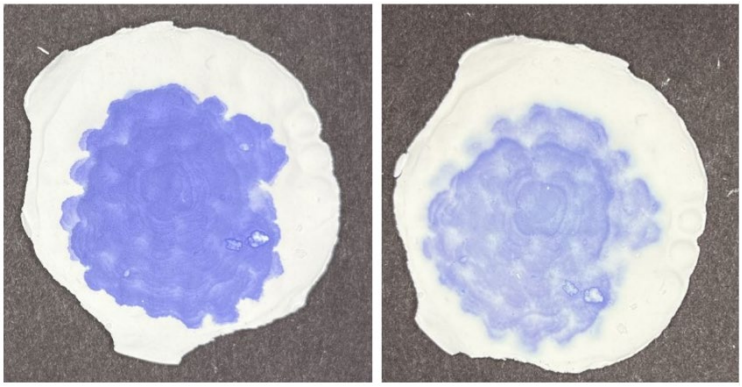

Figure A6: Right-0 min; Left-60 min

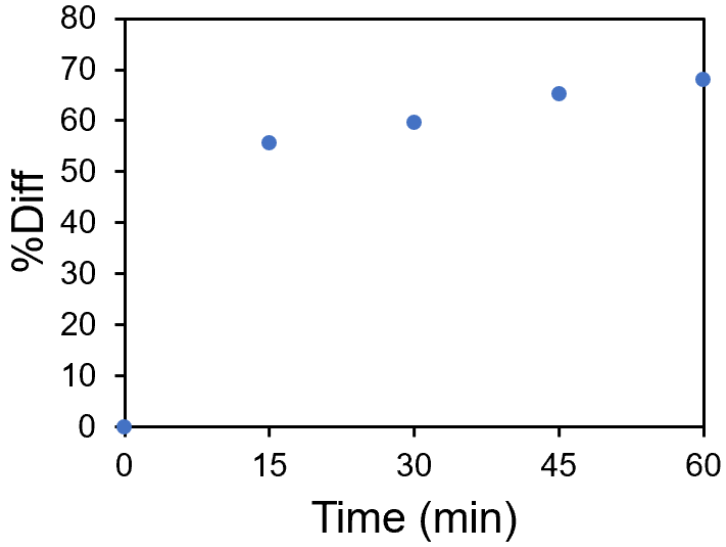

Figure A7: % Difference in methylene blue GV over time.

This qualitative study indicated that artificial light yielded a slightly more efficient breakdown of methylene blue. This was most likely due to a higher power of the source. Standardizing image capture is a crucial first step in collecting quantitative data. It was impossible to ensure that each image was taken at an identical distance and angle. This affected the standard deviations for the background, droplet size and shape, and even the tint of the image. Non-uniform distribution can be a source of error because the analysis necessitates measuring the Mean Grey

Value, which is the color intensity over the area of the highlighted region. This experimental error was resolved by utilizing the mass of the deposited dye as opposed to the concentration of the dye and by manually outlining each droplet. Mass is a more reliable variable than concentration for this study as it is independent of volume of solvent. This is an important distinction to be made because previous studies have revealed that evaporation of the solvent occurs. Though this evaporation is not quantifiable, any decrease in volume results in an increase of concentration. This increase of concentration was then correlating to and decrease in color intensity, which is not reasonable.

A5. Behavior of Dye on Filter Paper with No Light – A Control Experiment

As a control experiment, the purpose of this experiment was to verify any changes in the concentration of methylene blue over time due to a dark redox reaction on the filter paper that is . By utilizing filter paper, redox reactions occurring due to the catalytic surface's interaction with methylene blue, air, and water vapor was eliminated. Two droplets were analyzed and will be the focus of this discussion. What resulted was minimal change in mass between the initial and final time stamps. The slope was negative, but very small. This indicated there was an almost imperceptible change in concentration over time (Figure 16). A variation was observed in each measured mass; however, there was no apparent behavior that followed for 0^{th}, 1^{st}, or 2^{nd} order L-H kinetics. This experiment demonstrated that methylene blue does not oxidize with the air to form a detectable decrease of methylene blue in the dark experiment. Therefore, this control experiment was a success. Future work could include a control experiment of this nature for an extended period if experiments last longer than 5 m.

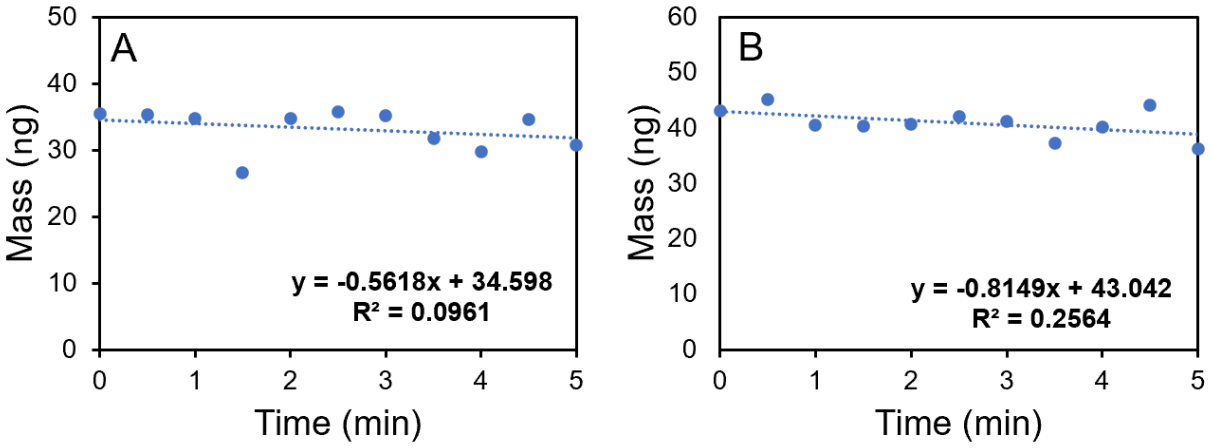

Figure A8: Methylene blue behavior over time on filter paper. No apparent kinetic behavior observed. (A) 36.3 ng droplet (B) 49.6 ng droplet.

Appendix B: Experimental Conditions, Spectra, and Additional Plots

Table B1: Gel Imaging System settings of the 4 experimental conditions

Settings	TiO_2 Dark	TiO_2 Light	Ag/TiO_2 Dark	Ag/TiO_2 Light
White Light	OFF	ON	OFF	ON
Trans Lighting	OFF	OFF	OFF	OFF
Emission Filter	Clear	Clear	Clear	Clear
Brightness	40%	40%	40%	40%
Focus	69%	69%	69%	69%
Noise Reduction	ON	ON	ON	ON
Exposure Time*	50 msec	50 msec	150 msec	150 msec
Epi Lighting	White	White	White	White

*Exposure time is the amount of time the camera lens is exposed to the photons emitted from the sample. The greater the exposure time, the more light is absorbed by the camera. This results in a brighter image.

Table B2: Power densities of selected wavelengths in 4 experimental conditions

Wavelength	Power Density TiO_2 Dark	Power Density TiO_2 Light	Power Density Ag/TiO_2 Dark	Power Density Ag/TiO_2 Light
320 nm	0 mW/cm^2	0 mW/cm^2	0 mW/cm^2	0 mW/cm^2
365 nm	0 mW/cm^2	0 mW/cm^2	0 mW/cm^2	0 mW/cm^2
405 nm	0 mW/cm^2	0.0398 mW/cm^2	0 mW/cm^2	0.0398 mW/cm^2
488 nm	0 mW/cm^2	0.0318 mW/cm^2	0 mW/cm^2	0.0318 mW/cm^2

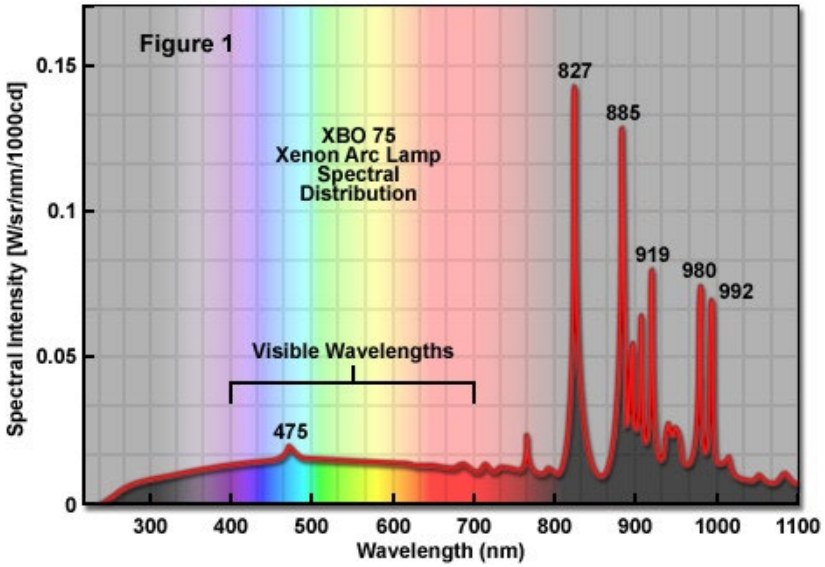

Figure B1: Spectrum of white light in Gel Imager System

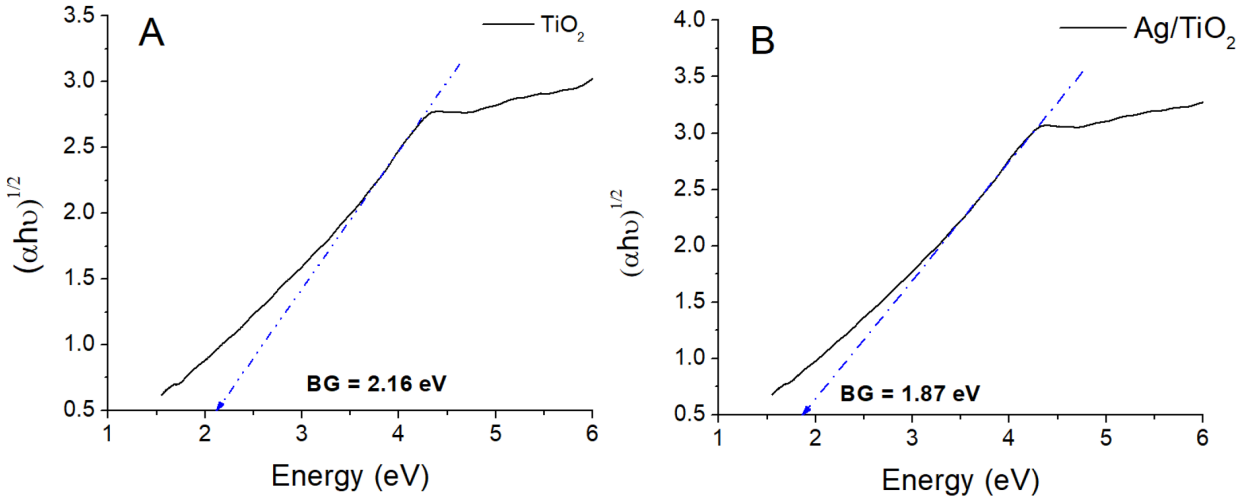

Figure B2: Tauc plot of indirect band gap.

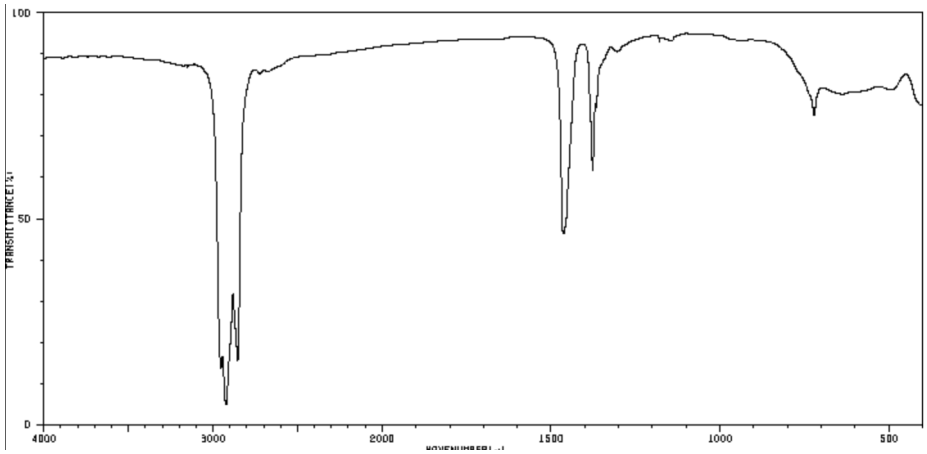

Figure B3: FTIR of TiO_2 taken from SDBS.

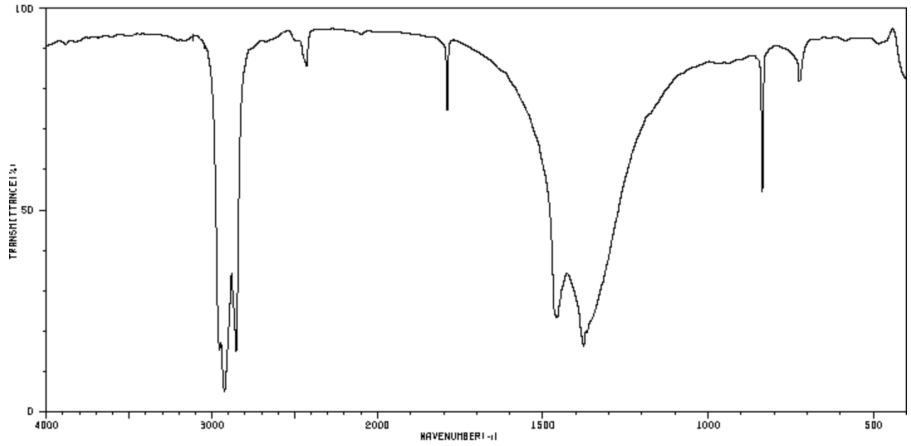

Figure B4: FTIR of $NaNO_3$ taken from SBDS.

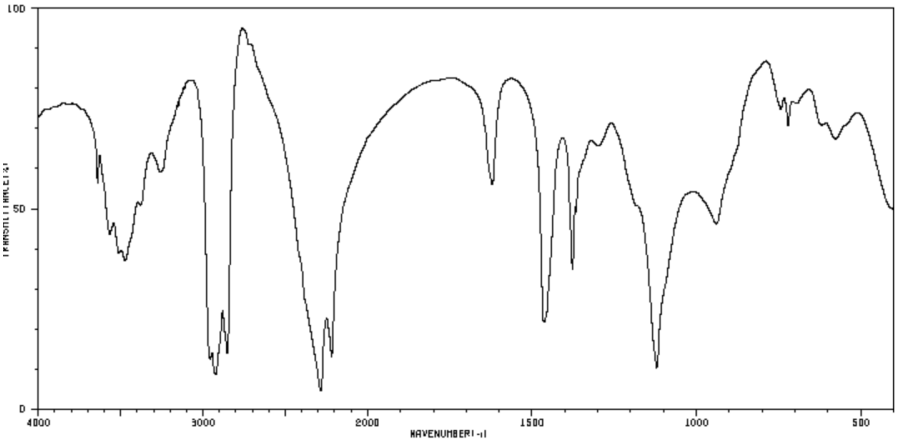

Figure B5: FTIR of $NaBH_4$ taken from SDBS.

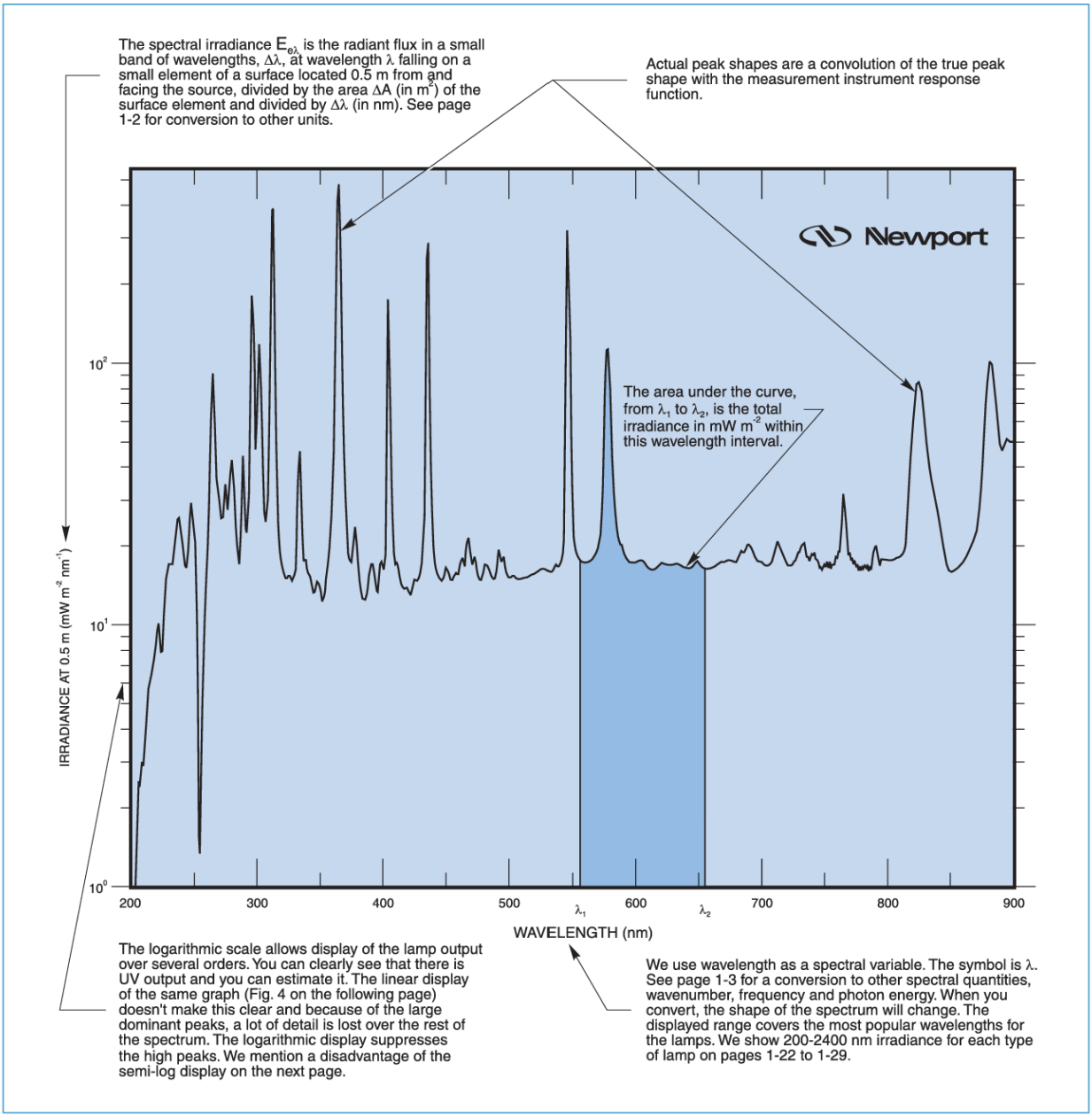

Fig. 3 Example of the spectral irradiance curves we show for our arc, quartz tungsten halogen, and deuterium lamps, on pages 1-22 to 1-30.

Figure B6: Artificial sunlight lamp spectrum

Appendix C: Derivations, Calculations, and Mechanisms

$$E_g = hv$$

$$E_g = \frac{hc}{\lambda}$$

$$E_g = \frac{19.85 \times 10^{-26} J \cdot m}{\lambda} = \frac{12.393 \times 10^{-7} eV \cdot m}{\lambda}$$

$$E_g = 1240 \frac{eV \cdot nm}{\lambda}$$

Zeroth Order Kinetics

$$Rate = -\frac{d[A]}{dt} = k[A]^0$$

$$\frac{d[A]}{dt} = -k$$

$$d[A] = -kdt$$

$$\int_{[A]_0}^{[A]} d[A] = -k \int_{t_0}^{t_1} dt$$

$$\boldsymbol{[A] - [A]_0 = -kt}$$

First Order Kinetics

$$Rate = -\frac{d[A]}{dt} = k[A]$$

$$\frac{d[A]}{dt} = -kdt$$

$$\int_{[A]_0}^{[A]_t} \frac{d[A]}{[A]} = \int_0^t -kdt$$

$$ln\frac{[A]_t}{[A]_0} = -kt$$

$$\boldsymbol{[A]_t = [A]_0 e^{-kt}}$$

$$where,$$

$$Slope = -k = 0.1477\ min^{-1}$$

$$R = 0.1477\ min^{1}(49.6\ ng) = \mathbf{7.33\ ng/min}$$

Second Order Kinetics

$$Rate = -\frac{d[A]}{dt} = k[A]^2$$

$$\frac{d[A]}{dt} = -kdt$$

$$-\int_{[A]_0}^{[A]} \frac{d[A]}{[A]^2} = \int_{t=0}^{t} kdt$$

$$-\frac{dx}{x^2} = d\left(\frac{1}{x}\right)$$

$$\mathbf{\frac{1}{[A]} - \frac{1}{[A]_0} = kt}$$